



**HAL**  
open science

# Magnus-Effect Winged Hybrid UAV System: Improved Energy Efficient and Autonomy Through Control Allocation Strategy

Zakeye Azaki, Jonathan Dumon, Alexis Offermann, Nacim Meslem, Pierre Susbielle, Amaury Nègre, Ahmad Hably

► **To cite this version:**

Zakeye Azaki, Jonathan Dumon, Alexis Offermann, Nacim Meslem, Pierre Susbielle, et al.. Magnus-Effect Winged Hybrid UAV System: Improved Energy Efficient and Autonomy Through Control Allocation Strategy. IEEE Transactions on Aerospace and Electronic Systems, 2024, pp.1-20. 10.1109/TAES.2024.3464569 . hal-04754019

**HAL Id: hal-04754019**

**<https://hal.science/hal-04754019v1>**

Submitted on 25 Oct 2024

**HAL** is a multi-disciplinary open access archive for the deposit and dissemination of scientific research documents, whether they are published or not. The documents may come from teaching and research institutions in France or abroad, or from public or private research centers.

L'archive ouverte pluridisciplinaire **HAL**, est destinée au dépôt et à la diffusion de documents scientifiques de niveau recherche, publiés ou non, émanant des établissements d'enseignement et de recherche français ou étrangers, des laboratoires publics ou privés.

# Magnus-Effect Winged Hybrid UAV System: Improved Energy Efficient and Autonomy Through Control Allocation Strategy

Zakeye AZAKI  
Jonathan DUMON  
Alexis OFFERMANN  
Nacim MESLEM  
Pierre SUSBIELLE  
Amaury NEGRE  
Ahmad HABLY

University Grenoble Alpes, CNRS, Grenoble INP, GIPSA Lab,  
Grenoble, France

**Abstract**—While multirotor unmanned aerial vehicles have excellent maneuverability, they lack the ability to perform long-endurance flights. Many design-based approaches to addressing this drawback exist. To overcome this challenge, this article proposes the Magnus-effect winged quadcopter system design. We use the rotational speed of the Magnus-effect based wings in this system as a control variable to maximize the contribution from these wings, thus minimizing the necessary and required thrust from the quadcopter and, therefore, the system’s energy consumption. To this end, we developed an airspeed-dependent nonlinear optimization control allocation scheme to operate the system at a wide range of airspeeds. Realistic simulations and outdoor experiments validate the approach, demonstrating the superior energy efficiency of the Magnus-based quadcopter system compared to traditional quadcopter and emphasizing its potential for achieving extended endurance.

**Index Terms**—Control allocation, hybrid UAV, Magnus effect technology, nonlinear modeling

## I. INTRODUCTION

In recent years, unmanned aerial vehicles (UAVs) have become increasingly prevalent across various industries and applications. As UAV flight missions become more complex, requirements are getting higher and higher. Developing UAVs that can fly longer distances and perform

*The corresponding author is Zakeye AZAKI.*

Authors’ addresses: Authors are with GIPSA-lab - Domaine Universitaire, 11 rue des Mathématiques, 38402 Saint-Martin d’Hères, France. E-mail: (zakeye.azaki@grenoble-inp.fr; jonathan.dumon@gipsa-lab.fr; alexis.offermann@grenoble-inp.fr; nacim.meslem@grenoble-inp.fr; pierre.susbielle@grenoble-inp.fr; amaury.negre@gipsa-lab.fr; ahmad.hably@grenoble-inp.fr).

more complex tasks is an ongoing challenge, and their power consumption is one of the main factors affecting their range and endurance. Therefore, research is widely carried out: on the one hand, on the hybrid energy UAVs [1], and on the other hand, on hybrid design UAVs [2], [3]. UAV platforms can generally be separated into two categories: fixed-wing UAVs and vertical take-off and landing (VTOL) UAVs such as helicopters and multirotor platforms [4]. In addition to their advantages, each type has its own limitations. In general, fixed-wing UAVs offer greater cruising speed, flight range, and endurance performance. However, runways are required for reliable takeoff and landing. Additionally, it is not applicable to missions requiring ultra-low flight speeds. Vertical takeoff and landing (VTOL) UAVs, on the other hand, have much looser requirements for takeoff and landing phases. A unique hovering capability further enhances its versatility in executing missions. However, the speed and endurance significantly limit the VTOL UAV’s capability in missions requiring wide-range coverage or long endurance.

As such, designing an aerial system that integrates the advantages of both fixed-wing and VTOL UAVs has long been a concern for the aerospace and aviation industries. The hybrid UAV, or fixed-wing VTOL UAV, was born out of such a demanding need. The most common hybrid UAVs found in the modern scientific literature are classified into three main categories: A tail-sitter typically has rotors rigidly connected to the airframe [5]. Thus, it changes the orientation of the entire vehicle when transitioning from VTOL orientation to horizontal flight. A tilt-rotor has multiple rotors mounted on a titling shaft. In this case, hover-to-cruise transitions commonly involve partial or all rotors tilting in the direction of flight to maintain forward speed until cruise flight is achieved [6]. Finally, tilt-wing VTOL UAVs, such that the rotors are fixed to the wings, and the entire wing rotates, with the fuselage mostly maintaining a horizontal position during flight [7]. Making hybrid UAVs fly as efficiently and safely as possible poses a number of challenges. These include dealing with large flight envelopes, over-actuation, its non-linear nature, and its sensitivity to wind gusts.

As a result of the nonlinear dynamics resulting from the interaction of different aerodynamic effects, the automatic control of hybrid UAVs is still a challenge today. It is essential for the flight controller to be able to handle potentially large changes in angle of attack, velocity, attitude, and actuator control effectiveness depending on airspeed, which all have an impact on the vehicle’s aerodynamic forces and torques. The primary design goal of fixed-wing VTOL UAVs is to use the wing aerodynamic force as the lift during cruising (or level flight). As a result, the position control (or velocity control) loop has to consider the aerodynamic forces in determining the attitude and thrust. For the design of robust controllers, an insufficient understanding of aerodynamic forces acting on aircraft dynamics is particularly challenging. For instance, in [8], the proposed control design methodology utilizes a simple aerodynamic force model for the system,

representative of environmental physics and conducive to control design, with minimal assumptions about the sideslip transversal component and unrestricted attack angles, complemented by bounded integral actions to address modeling errors. The model acknowledges its limitations beyond a certain attack angle, where stall phenomena become abrupt and complex. In contrast, [9] reported a nonlinear, sequential convex programming optimization problem to control a tail-sitter UAV in all flight modes. This achievement enables the determination of reference attitude and thrust, leveraging a precise aerodynamic model established through comprehensive wind tunnel testing across the full flight envelope. Li *et al.* [10] proposed a nonlinear robust control design method for tail-sitter UAVs where the control law is based on the dynamic inversion technique to incorporate fixed-wing aerodynamics. Based on a simplified aerodynamic model of the fixed wing, a model predictive control (MPC) as a velocity control loop for tilt-rotor VTOL UAVs has been designed in [11], [12]. These articles implemented a control allocation to allocate torques between the aerodynamic and quadcopter actuators. In [13], [14], a fully automated flight control system is proposed for tilt-wing UAV. In these articles, the propeller-wing aerodynamic interaction is addressed and considered.

In all the aforementioned works, the torques required to control the system's attitude were allocated and mapped between all the existing actuators. However, the required thrust from the quadcopter, which could be related to power consumption, is not optimized. Willis *et al.* [15] implemented a thrust optimization aligned with pitch optimization. This was done under the assumption of no external wind. Thus, the angle of attack and, in turn, the aerodynamic forces can be easily related to the system's pitch angle. However, for windy scenarios, this approach will require precise estimation of the wind speed direction, which is generally not an easy task. Our present research aligns closely with the work presented in the aforementioned article, as both studies focus on optimizing the thrust. In contrast, we employed wings based on the Magnus effect instead of fixed wings to achieve our objectives. This novel strategy adds a unique dimension to our research, offering potential advantages over traditional control surfaces. These include the speed and direction of rotation of the Magnus-effect based wing, which can be controlled easily and robustly to create the desired aerodynamic lift independently on the angle of attack, thereby providing greater control over the flight path of an aircraft. The Magnus effect, experiencing a resurgence in the past century, offers a promising departure from traditional lifting devices. Studies show Magnus-effect based wings outperform classical airfoils, with around eight times higher lift coefficients, necessitating more compacted surface area for the same lift. However, this comes at the cost of a lower lift-to-drag coefficient, as observed in the aerodynamic data comparison of NACA airfoils and Magnus-effect based wings in [16], [17]. This phenomenon has inspired rotor-based solutions in



Fig. 1: Magnus-effect winged quadcopter system (MWQ). The gray cylinders are the Magnus-effect based wings. The quadcopter's four rotors are attached to the arm extensions. A short video of one of the outdoor experiments is available at <https://youtu.be/dtGctfuA6s>

the realm of fuel-efficient ship propulsion and the design of rotor airplanes, incorporating combined lifting devices [18]. In this context, it is also pertinent to highlight recent advancements in the study and application to incorporate the Magnus effect into Airborne Wind Energy systems, as explored in works such as [19], [20]. Our work explores the Magnus effect's role in cutting-edge aviation technologies, suggesting its potential to enhance flight autonomy.

In this work, we present a novel hybrid UAV that is composed of a quadcopter as an actuation necessary for vertical take-off and landing maneuvers and a Magnus-effect based wing airframe that has some sort of wing capable of generating aerodynamic lift forces at sufficient forward speed. This work presents our novel system, the Magnus-effect winged quadcopter (MWQ) system. A nonlinear optimization-based controller is developed based on a nonlinear dynamical model of the vehicle considering the aerodynamic model of the Magnus-effect based wings. This control strategy aims to allocate the control commands between the quadcopter propulsion system and the Magnus lifting system. The redundancies between rotors and Magnus aerodynamic actuators must be adequately employed because the control authority depends on the flight conditions. For example, the Magnus actuators have more control authority as the airflow speed passes over them increases. Flight tests were performed to validate different aspects of this study.

**The contributions of this paper are:** (i) design of a novel Magnus-effect winged quadcopter system; (ii) establish the model of a Magnus-effect winged quadcopter system, which includes the experimentation-based estimation and identification of quadcopter's propellers and aerodynamic models; (iii) optimization-based control allocation for energy-saving performance. Comprehensive outdoor experiment tests are performed to show (a) the proposed Magnus-effect winged quadcopter can be more energy-saving than the Magnus-free quadcopter; (b) the system's performance at different flying speeds.

## A. Magnus-effect winged Quadcopter (MWQ) System Architecture

Fig. 1 shows an overview of the developed Magnus-effect winged quadcopter system. The Magnus-effect based wings are attached to the quadcopter on the left and right. One can mention some mechanical drawbacks of the system, which are comparable to the fixed-wing VTOL UAVs. For example, the rotating actuators of the two Magnus-effect based wings induce additional dead weight, which requires additional power consumption in the hovering mode. Moreover, the exposed surface area of these wings during take-off and landing increases the sensitivity to wind, but this area is more compressed compared to the case of tail-sitter and tilt-wing VTOL UAVs. One aspect that must be considered is the interaction between the quadcopter's slipstream and the Magnus-effect based wings. Therefore, placing the Magnus-effect based wings in an area where the propeller slipstream does not affect its control performance is crucial [21], [22]. Consequently, arm extensions have been incorporated to attach the quadcopter's rotors at a distance from the rotating Magnus-effect based wings.

## B. Paper Organization:

The paper is structured as follows: in Section II, we present the full dynamical model of the system. In Section III, we delve into estimating process of the quadcopter's propeller performance and fuselage aerodynamic models. Moving on to Section IV, we elaborate on the outer position control loop designed for the Magnus-free quadcopter system. The main contribution of this paper, the optimization-based control allocation strategy, is detailed in Section V. In Section VI, we present and discuss the experimental results. Finally, we conclude with insights and future directions in Section VII.

## II. MWQ System Dynamical Model

### A. Reference Frames

The subsequent reference frames are defined to develop the equations of motion. These frames are represented in Fig. 2a,

- Inertial Frame  $\mathcal{I}(I, \mathbf{x}_i, \mathbf{y}_i, \mathbf{z}_i)$ , the origin point  $I$ , is considered as the reference for position measurements.
- Quadcopter Body Frame  $\mathcal{Q}(Q, \mathbf{x}_q, \mathbf{y}_q, \mathbf{z}_q)$ , the origin  $Q$  coincides with the center of mass of the quadcopter. The vectors  $\mathbf{x}_q$ ,  $\mathbf{y}_q$ , and  $\mathbf{z}_q$  are parallel to the principal axes of the moment of inertia, with  $\mathbf{x}_q$  (resp.  $\mathbf{y}_q$ ) is along the longitudinal (resp. lateral) axis of the quadcopter and  $\mathbf{z}_q$  is pointing upward.
- Right Magnus Cylinder Frame  $\mathcal{M}_r(M_r, \mathbf{x}_r, \mathbf{y}_r, \mathbf{z}_r)$ , the origin  $M_r$  is aligned with the center of mass of the right Magnus cylinder. The vector  $\mathbf{y}_r$  is oriented in the opposite sense of the right Magnus cylinder's rotation axis.

- Left Magnus Cylinder Frame  $\mathcal{M}_l(M_l, \mathbf{x}_l, \mathbf{y}_l, \mathbf{z}_l)$ , the origin  $M_l$  aligns with the center of mass of the left Magnus cylinder. The vector  $\mathbf{y}_l$  is oriented in the opposite sense of the left Magnus cylinder's rotation axis.
- Body Frame  $\mathcal{B}(B, \mathbf{x}_b, \mathbf{y}_b, \mathbf{z}_b)$ , The origin  $B$  is set at the center of mass of the combined Magnus-effect winged quadcopter system. The base vectors are parallel to those of the quadcopter body frame  $\mathcal{Q}$ . This frame is considered the body frame supporting all other spinning bodies.

For the seek of simplicity, we denote the frames  $\mathcal{I}$ ,  $\mathcal{Q}$ ,  $\mathcal{M}_r$ ,  $\mathcal{M}_l$ ,  $\mathcal{B}$  as  $i$ ,  $q$ ,  $r$ ,  $l$  and  $b$  respectively. The pitch, yaw, control, and desired frames, described when used, are denoted by  $p$ ,  $y$ ,  $c$ , and  $d$ , respectively, as introduced and described in their relevant contexts. Throughout this paper, a matrix  $R_a^b = [\mathbf{x}_a^b, \mathbf{y}_a^b, \mathbf{z}_a^b] \in SO(3)$  represents the rotation matrix that rotates any vector in  $a$  frame into  $b$  frame. Its inverse is  $R_b^a$ . The vector notation  ${}^a\mathbf{F}_b^c$  denotes a force of nature  $a$ , generated by the system's component  $b$ , and expressed in frame  $c$ . For example the case where  ${}^D\mathbf{F}_r^i$  corresponds to drag force of the right Magnus cylinder expressed in inertial frame  $\mathcal{I}$ . The notation  $\mathbf{r}_{a/b}^c$  denotes a vector quantity  $\mathbf{r}$  of frame  $a$  with respect to frame  $b$  and expressed in frame  $c$ . The quantities  $r_{x,a/b}^c$ ,  $r_{y,a/b}^c$ , and  $r_{z,a/b}^c$  represents the components of  $\mathbf{r}_{a/b}^c$ . The vectors are represented by bold formatting. The transpose of any vector  $\mathbf{r}$  is denoted by  $\bar{\mathbf{r}}$ . We define the operator  $[\mathbf{r}]_{\times}$  which forms a  $3 \times 3$  skew matrix from the vector  $\mathbf{r} \in \mathbb{R}^3$ . The notation  $\|\cdot\|$  denotes the Euclidean norm of a vector,  $\cdot^2$  denotes the element-wise square of a vector,  $\times$  denotes the cross product between vectors, and  $*$  denotes matrix multiplication.

### B. Modeling

Let  $\mathbf{p}_{b/i}^i \in \mathbb{R}^3$ , and  $\mathbf{v}_{b/i}^i$  be respectively the position and velocity of MWQ system with respect to the inertial frame  $\mathcal{I}$ ,  $\mathbf{w}_{b/i}^b \in \mathbb{R}^3$  represents the angular velocity of the system with respect to the inertial frame  $\mathcal{I}$  and represented in the body frame  $\mathcal{B}$ . The apparent speed is denoted by  $\mathbf{v}_a$ . Considering  $\mathbf{v}_w$  as the wind velocity vector, we have

$$\mathbf{v}_a = \mathbf{v}_{b/i} - \mathbf{v}_w \quad (1)$$

It is crucial to note that due to the unavailability of a wind speed sensor, all the studies, analyses, and tests conducted in this work are considering the following conservative assumption

ASSUMPTION 1. *No external wind exists. In other words, the apparent speed  $\mathbf{v}_a = \mathbf{v}_{b/i}$  based on (1)*

We denote  $m$  as the mass of the system,  $J_b \in \mathbb{R}^{3 \times 3}$  as the inertia matrix, and  $\mathbf{g}$  as the acceleration vector due to gravity. The matrix  $R_i^b \in SO(3)$  is the matrix that rotates inertial frame vectors into the body frame.  $R_i^b$  is composed of three rotations by the so-called Euler angles: roll, pitch, yaw or  $\phi$ ,  $\theta$ ,  $\psi$  respectively, in the  $ZYX$  intrinsic formulation,

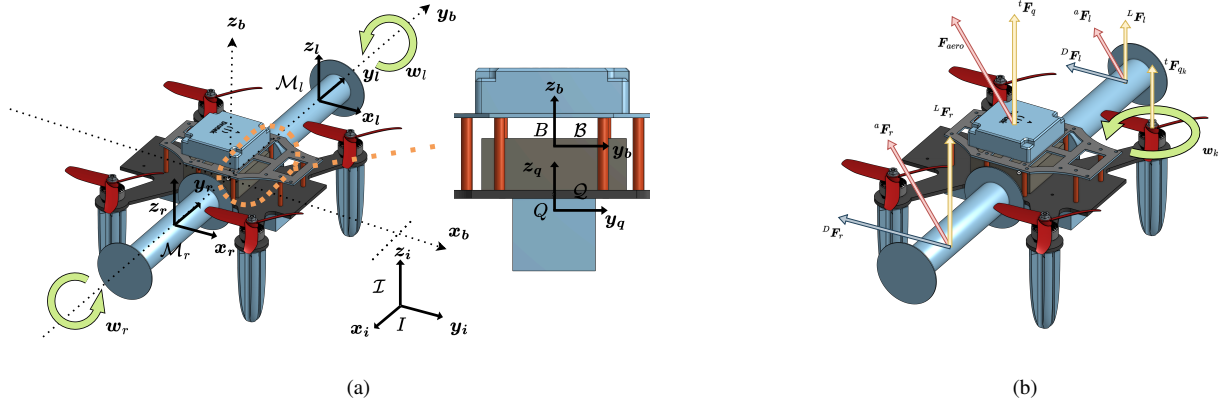


Fig. 2: (a) Frame definition on the system. From the figure,  $\mathcal{B}$  represents the body frame,  $\mathcal{Q}$  the quadcopter body frame,  $\mathcal{M}_r$  and  $\mathcal{M}_l$  respectively the right and left Magnus frame, and  $\mathcal{I}$  the inertial frame. (b) Forces acting on the system. From the figure,  ${}^t\mathbf{F}_{qk}$  is the thrust force generated by  $k^{th}$  propeller of the quadcopter  ${}^t\mathbf{F}_q$  is the total thrust generated by the quadcopter, and  $\mathbf{F}_{aero}$  is the total aerodynamic force of the Magnus-effect based wings.

$$R_i^b := R_i^b(\phi, \theta, \psi) = R_p^b(\phi) * R_y^b(\theta) * R_z^b(\psi) \quad (2)$$

We assume that the centers of mass are mutually fixed, the body structure is rigid, the system is yaw stable, and the mass and moments of inertia are constant. The translational dynamical equations are formulated using Newton's law of clustered bodies respectively:

$$\begin{aligned} \dot{\mathbf{p}}_{b/i}^i &= \mathbf{v}_{b/i}^i \\ \dot{\mathbf{v}}_{b/i}^i &= \mathbf{g}^i + \frac{1}{m} R_i^b \mathbf{F}_b^b \end{aligned} \quad (3)$$

The translational dynamics state variables correspond to the system's linear and angular velocities w.r.t. inertial frame  $\mathcal{I}$ , respectively:

$$\mathbf{v}_{b/i}^i = \dot{\mathbf{p}}_{b/i}^i = \begin{bmatrix} \dot{p}_{x,b/i}^i \\ \dot{p}_{y,b/i}^i \\ \dot{p}_{z,b/i}^i \end{bmatrix} \quad (4)$$

such that  $\mathbf{F}_b^b = [F_{x,b}^b, F_{y,b}^b, F_{z,b}^b]^T$  is the vector of the forces acting on the system in the body frame. In addition to the system's weight, the forces acting on the MWQ system are divided into two distinct components: first, the aerodynamic forces acting on the airframe; second, we have the forces produced by the rotors. In the subsequent subsections, we will comprehensively describe the forces acting on the system. For moments consideration and more details on the forces acting on the system, the reader can refer to our paper [23]. Fig. 2b represents some of the forces acting on the system.

The main goal of our present work is to show the thrust consumption comparison of the quadcopter with that of the Magnus-effect winged quadcopter system. To this end, we must distinguish between two scenarios: the Magnus-free quadcopter scenario described in Subsection C. The other scenario is the Magnus-effect winged quadcopter scenario presented in Subsection D.

### C. Magnus-free Quadcopter Configuration

In this section, we describe, more in detail, the dynamics and the controller of the Magnus-free quadcopter system. This system is considered to be the quadcopter alone without the Magnus-effect based wings. In this case, the mass of the body  $m$  is the mass of the quadcopter  $m_q$ , i.e.,  $m = m_q$ , and the body frame  $\mathcal{B}$  coincident with that of the quadcopter  $\mathcal{Q}$ . The forces in the quadcopter component can be specified as follows,

- The thrust forces: are the forces generated by the rotation of each rotor  $k \in \{1, 2, 3, 4\}$  perpendicular to the axis plane and proportional to the rotor's rotational speed  $w_k$ :

$${}^t\mathbf{F}_{qk}^b = c_T w_k^2 \mathbf{z}_b = T_k \mathbf{z}_b \quad (5)$$

where  $c_T > 0$  is the thrust coefficient. Therefore, the thrust force generated by the four propellers can be computed as

$${}^t\mathbf{F}_q^b = \sum_k {}^t\mathbf{F}_{qk}^b = c_T \sum_k w_k^2 \mathbf{z}_b = T \mathbf{z}_b \quad (6)$$

with  $T = \sum_k T_k$  being the total thrust force magnitude generated by the four propellers. The thrust force model in (6) holds if we ignore the fact that aerodynamic forces can significantly affect the propellers' performance, which in turn affects its performance. To this end, we can rewrite the total thrust force as,

$${}^T\mathbf{F}_q^b = {}^t\mathbf{F}_q^b + {}^p\mathbf{F}_{xy,q}^b + {}^p\mathbf{F}_{z,q}^b \quad (7)$$

The net force  ${}^p\mathbf{F}_{xy,q}^b$  is in the horizontal plane of the rotors. We based on [24] to model this component of thrust force as

$${}^p\mathbf{F}_{xy,q}^b = -k_p \sum_k w_k \mathbf{v}_{xy,b/i}^b \quad (8)$$

where  $k_p$  is a positive coefficient known as rotor drag coefficient and  $\mathbf{v}_{xy,b/i}^b$  is the projection of  $\mathbf{v}_{b/i}^b$

on the propeller plane. In what follows, we assume  $\lambda_p = k_p \sum_k w_k$  is a positive constant considering the fact that the summation of propeller rotational rates is relatively constant during a smooth flight. The force  ${}^p \mathbf{F}_{z,q}^b$  reflects the influence of aerodynamic factors and efficiency on the propeller's performance. As the apparent speed changes, the propeller's angle of attack and the airflow over its blades also change, affecting its efficiency. The thrust coefficient takes into account these aerodynamic variations

$${}^p \mathbf{F}_{z,q}^b = c'_T \sum_k w_k^2 \mathbf{z}_b \quad (9)$$

such that  $c'_T := c'_T(v_{z,b/i}^b)$  is a velocity dependent propeller performance coefficient. The total thrust in (7) can be rewritten as,

$${}^T \mathbf{F}_q^b = \left( c_T + c'_T(v_{z,b/i}^b) \right) \sum_k w_k^2 \mathbf{z}_b + {}^p \mathbf{F}_{xy,q}^b \quad (10)$$

- The aerodynamic forces acting on the quadcopter body: the forces generated are due to the system motion through the apparent speed. We choose to model these forces as three drag forces described in body frame  $\mathcal{B}$  as,

$$\begin{cases} {}^D F_{x,q}^b = -\frac{1}{2} \rho S_{x,q} c_{D_{x,q}} \left( v_{x,b/i}^b \right)^2 \\ {}^D F_{y,q}^b = -\frac{1}{2} \rho S_{y,q} c_{D_{y,q}} \left( v_{y,b/i}^b \right)^2 \\ {}^D F_{z,q}^b = -\frac{1}{2} \rho S_{z,q} c_{D_{z,q}} \left( v_{z,b/i}^b \right)^2 \end{cases} \quad (11)$$

such that  $c_{D_{x,q}}$ ,  $c_{D_{y,q}}$  and  $c_{D_{z,q}}$  are the quadcopter's drag coefficients along the axes  $\mathbf{x}_b$ ,  $\mathbf{y}_b$  and  $\mathbf{z}_b$  respectively, similarly  $S_{x,q}$ ,  $S_{y,q}$ , and  $S_{z,q}$  are the cross-section quadcopter's areas towards the air.

The identification processes of the quadcopter's constant coefficients, based on experiment tests, are describe in following Section III.

#### D. Magnus-effect winged Quadcopter Configuration

In addition to the forces acting on the quadcopter, as detailed in Subsection C, the MWQ system incorporates forces acting on the Magnus-effect based wings. Forces in the lifting Magnus-effect based wings component can be described as follows,

- The aerodynamic characteristics of the Magnus-effect based wings are affected by various factors. The most important one that controls the Magnus-effect based wing is its spin ratio  $X$ , such that for each Magnus-effect based wing  $k \in \{r, l\}$

$$X_k = \frac{R_k \|\mathbf{w}_{k/b}^b\|}{\|\mathbf{v}_{b/i}\|} \quad (12)$$

where  $R_k$  is the radius of each Magnus cylinder  $k \in \{r, l\}$  and  $\mathbf{w}_{k/b}^b$  is the rotational velocity of each Magnus cylinder  $k \in \{r, l\}$  with respect to body

frame  $\mathcal{B}$ . The drag  $c_{D_k}$  and lift  $c_{L_k}$  coefficients are modeled such that

$$\begin{cases} c_{D_k} := c_{D_k}(\mathbf{w}_{k/b}, \mathbf{v}_{b/i}) := c_{D_k}(X_k) \\ c_{L_k} := c_{L_k}(\mathbf{w}_{k/b}, \mathbf{v}_{b/i}) := c_{L_k}(X_k) \end{cases} \quad (13)$$

We then define the longitudinal aerodynamic drag and lift forces according to [25] to be

$$\begin{aligned} {}^D \mathbf{F}_k^b &= \frac{1}{2} \rho S_k c_{D_k} \|\mathbf{v}_{xz,b/i}\|^2 \mathbf{e}_{D_k} \\ {}^L \mathbf{F}_k^b &= \frac{1}{2} \rho S_k c_{L_k} \|\mathbf{v}_{xz,b/i}\|^2 \mathbf{e}_{L_k} \end{aligned} \quad (14)$$

with  $S_k$  represents the projected surface area of each Magnus-effect based wing  $k \in \{r, l\}$ . The directions of the drag and lift forces for each Magnus-effect based wing  $k \in \{r, l\}$  are defined such that the drag force aligns with the apparent speed, which is  $\mathbf{v}_a = \mathbf{v}_{b/i}$  according to Assumption 1, and the lift force is orthogonal to the Magnus-effect based wing's axis of rotation and the apparent wind velocity. This leads to:

$$\begin{cases} \mathbf{e}_{D_k} = -\frac{\mathbf{v}_{b/i}}{\|\mathbf{v}_{b/i}\|} \\ \mathbf{e}_{L_k} = \mathbf{y}_k \times \mathbf{e}_{D_k} \end{cases} \quad (15)$$

Lastly, the total aerodynamic forces of each Magnus-effect based wing are read as follows:

$$\begin{cases} {}^a \mathbf{F}_r^b = {}^D \mathbf{F}_r^b + {}^L \mathbf{F}_r^b \\ {}^a \mathbf{F}_l^b = {}^D \mathbf{F}_l^b + {}^L \mathbf{F}_l^b \end{cases} \quad (16)$$

The lateral aerodynamic force produced by each Magnus effect-based wing  $k \in \{r, l\}$ ,

$${}^y \mathbf{F}_k^b = \frac{1}{2} \rho S_{y_k} c_{D_{y_k}} \|\mathbf{v}_{y,b/i}^b\|^2 \mathbf{y}_k \quad (17)$$

where  $S_{y_k}$  and  $c_{D_{y_k}}$  are, respectively, the lateral surface area and the lateral drag coefficient of the  $k$ th Magnus-effect based wing.

The nonlinear model presented in this section is used in simulations to test the algorithm in a realistic simulator before testing in real experimentation. However, as described in the Section IV, the control design ignores the quadcopter's propeller drag, performance, and fuselage aerodynamic forces.

### III. Forces Identification

The identification processes of the quadcopter's thrust force model, the propellers' drag force model, the propellers' performance model, and the quadcopter's fuselage aerodynamic model are detailed in this section. This is an important step to construct a realistic simulator that can be used to test the system's performance before going into experimental testing.

#### A. Identification of Thrust Coefficient

Various estimation processes introduced in the preceding section rely on estimating thrust force accurately. The

thrust magnitude in (6) is modeled as,

$$T = c_T \sum_k w_k^2 [rd.s^{-1}] \quad (18)$$

where  $w_k [rd.s^{-1}]$  denotes the rotational speed of each propeller  $k \in \{1, 2, 3, 4\}$ . For data collection, propellers' speeds were collected from the embedded flight controller based on motor speeds setpoints sent to electronic speed controller (ESC). Experimental testing is conducted to gather empirical data on propeller speeds, consisting of systematic additions of 30g mass throughout the weight range of the quadcopter's base weight without Magnus to the full weight of the MWQ system. Similar experiments were carried out for lower weights, including low thrust scenarios, such as those encountered due to control allocation strategies, as shown in Section VI. The thrust coefficient  $\hat{c}_T = 2.4815e-06 [N.rd^{-2}.s^2]$  was estimated using a least squares identification approach. Results were validated using the Root Mean Square Error (RMSE) between the estimated thrust applied by the quadcopter as the ground truth reference and the interpolation performed on the modeled surface (18) obtained through the least square criterion. The validation process is repeated across the full weight range. The results are displayed in Fig. 3, which shows higher errors for bigger weights. We record the following main results:

- For weight of 1.244kg: RMSE = 0.0675N. This corresponds to a small thrust magnitude that we could reach, even lower, while controlling our system using the control allocation strategy at high-flying speeds.
- For weight of 1.496kg: RMSE = 0.0616N. This provides an overview of the weight of the base Magnus-free quadcopter system. The precision achieved in estimating the thrust model significantly enhances its trustworthiness, laying a solid foundation for its integration into the quadcopter's drag model estimation, which will be presented in the following subsection.
- For weight of 1.796kg: RMSE = 0.1988N. This provides an overview of the full weight of the MWQ system. The full weight of the MWQ system corresponds to the total weight of the Magnus-free quadcopter plus that of the Magnus cylinders, and the Magnus actuators.

For a comprehensive overview, we validate the thrust model (18) through Fig. 4 across the experimental tests. The black curve shows the actual measured weight of the system, the red dotted curve represents the thrust generated by the quadcopter that is used to compute the thrust model, this thrust values are estimated through offline Kalman Filter (KF), the blue curve represents the predicted quadcopter's thrust force according to the sum of square model (18) we computed. Comparing the blue curve to the red dotted curve, the curves exhibit a good fit. It's worth noting that there is a tendency for overestimating thrust, particularly noticeable at high weights, as depicted in the figure. However, this chosen thrust model is more accurate for lower weights, which

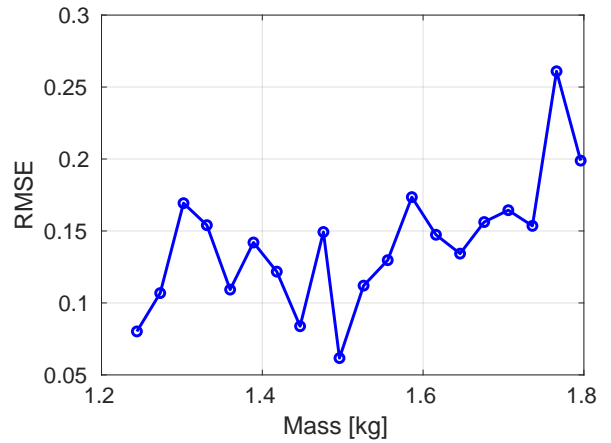


Fig. 3: Root mean square values between the actual thrust applied by the quadcopter as the ground truth reference and the thrust estimated according to the thrust model (18).

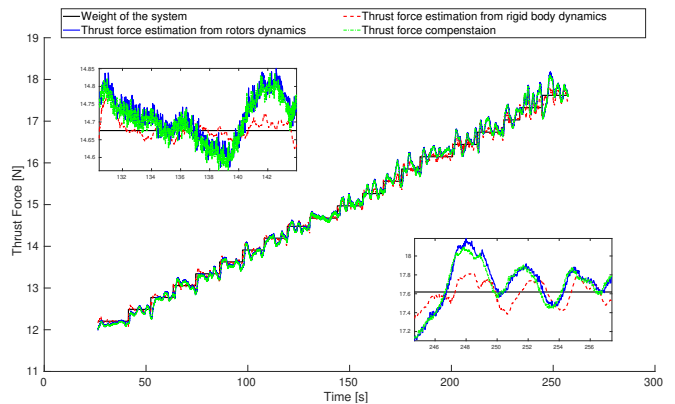


Fig. 4: Validation of propeller's thrust model. From the figure, the black line corresponds to the actual weights of the system, the red line corresponds to the estimated thrust, the blue line corresponds to the thrust predicted according to the square of the sum of rotors' rotational speed and  $\hat{c}_T$  (18), and the green line corresponds to the inverse of the compensated thrust according to (47).

corresponds to lower thrust forces in practice. This range is also more relevant to our study. Finally, the dotted green curve corresponds to the thrust force computed according to the inverse of (47) based on the normalized thrust measured forces. The accurate fit of the blue curve with the green dotted curve validate transition model from the desired thrust force in Newtons to the normalized thrust force fed to the autopilot. This will be represented lately through (47).

## B. Magnus-free Quadcopter System Identification

Performing a theoretical calculation for the constant coefficients of the quadcopter's aerodynamic and propellers' performance modeling is complex, so we opted for an offline experimental identification approach. To

achieve this, outdoor Magnus-free quadcopter flying experiment tests were conducted at various linear speeds  $exp \in \{2m.s^{-1}, 6m.s^{-1}, 8m.s^{-1}, 10m.s^{-1}\}$ . The fundamental methodology employed here involves the first step of independently estimating offline the overall disturbance force vector  $\mathbf{F}_q$  acting on the quadcopter during each Magnus-free quadcopter flying test. Then, the identification process is done based on data collected from stable regions of these distinct disturbance estimations.

The disturbance force  $\mathbf{F}_q$  could be viewed as a composition in between the forces  ${}^p\mathbf{F}_{xy,q}$  and  ${}^p\mathbf{F}_{z,q}$  reflecting the effect of aerodynamics on the quadcopter's propellers as in (8)-(9) and the aerodynamic force vector  ${}^a\mathbf{F}_q$  acting on the quadcopter body as in (11). Therefore, we can write,

$$\mathbf{F}_q = {}^a\mathbf{F}_q + {}^p\mathbf{F}_{xy,q} + {}^p\mathbf{F}_{z,q} \quad (19)$$

We consider that the forces acting on the body system are the gravity force  $\mathbf{g}$ , thrust force  ${}^t\mathbf{F}_q$ , and additive disturbance forces  $\mathbf{F}_q$ . Measuring the position  $\mathbf{p}_{b/i}^i$  of the quadcopter, the Euler angular positions  $\Theta = [\phi, \theta, \psi]^T$  and the rotors' rotational speed  $w_k$  for  $k \in \{1, 2, 3, 4\}$ , the additional forces acting on the system can be estimated as part of the states using KF [26]. To this end, an augmented model is considered in the design of the KF, such that,

$$\begin{aligned} \underbrace{\begin{bmatrix} \dot{\mathbf{p}}_{b/i}^i \\ \dot{\mathbf{v}}_{b/i}^i \\ \dot{\mathbf{F}}_q^i \end{bmatrix}}_{\mathbf{x}_o} &= \begin{bmatrix} \mathbf{0} & I_3 & \mathbf{0} \\ \mathbf{0} & \mathbf{0} & \frac{1}{m}I_3 \\ \mathbf{0} & \mathbf{0} & \mathbf{0} \end{bmatrix} \underbrace{\begin{bmatrix} \mathbf{p}_{b/i}^i \\ \mathbf{v}_{b/i}^i \\ \mathbf{F}_q^i \end{bmatrix}}_{\mathbf{x}_o} + \begin{bmatrix} \mathbf{0} \\ I_3 \\ \mathbf{0} \end{bmatrix} \underbrace{\left( \mathbf{g}^i + \frac{1}{m} R_b^{it} \mathbf{F}_q^b \right)}_{\mathbf{u}_o} \\ \mathbf{y}_o &= \mathbf{p}_{b/i}^i = [I_3 \quad \mathbf{0} \quad \mathbf{0}] \mathbf{x}_o \end{aligned} \quad (20)$$

System (20) is a linear observable system. Therefore, the measurements provided by the GPS receiver allow one to estimate the additional forces acting on the quadcopter. The estimated force vector  $\hat{\mathbf{F}}_q^i$  is represented in inertial frame  $\mathcal{I}$  and that in body frame  $\mathcal{B}$  is  $\hat{\mathbf{F}}_q^b = R_b^i \hat{\mathbf{F}}_q^i$ . The estimated additional force vector  $\hat{\mathbf{F}}_q^b$  can be formulated by combining (8), (9), and (11),

$$\begin{cases} \hat{F}_{x,q}^b = -\frac{1}{2}\rho S_{x,q} \hat{c}_{D_{x,q}} \left( v_{x,b/i}^b \right)^2 - \hat{\lambda}_p v_{x,b/i}^b \\ \hat{F}_{y,q}^b = -\frac{1}{2}\rho S_{y,q} \hat{c}_{D_{y,q}} \left( v_{y,b/i}^b \right)^2 - \hat{\lambda}_p v_{y,b/i}^b \\ \hat{F}_{z,q}^b = -\frac{1}{2}\rho S_{z,q} \hat{c}_{D_{z,q}} \left( v_{z,b/i}^b \right)^2 + \hat{c}'_T \sum_k w_k^2 \end{cases} \quad (21)$$

For the ease of generalization, we estimated the aerodynamic model by solving the following problem,

$$\begin{cases} \hat{F}_{x,q}^b = -\hat{c}_{x,q} \left( v_{x,b/i}^b \right)^2 - \hat{\lambda}_p v_{x,b/i}^b \\ \hat{F}_{y,q}^b = -\hat{c}_{y,q} \left( v_{y,b/i}^b \right)^2 - \hat{\lambda}_p v_{y,b/i}^b \\ \hat{F}_{z,q}^b = -\hat{c}_{z,q} \left( v_{z,b/i}^b \right)^2 + \left( \hat{\lambda}_{T_1} - \hat{\lambda}_{T_2} |v_{z,b/i}^b| \right) v_{z,b/i}^b \sum_k w_k^2 \end{cases} \quad (22)$$

such that we choose the second order polynomial model  $\hat{c}'_T(v_{z,b/i}^b) := \lambda_{T_1} v_{z,b/i}^b - \lambda_{T_2} |v_{z,b/i}^b| v_{z,b/i}^b$  to model the

influence of the aerodynamics on the propellers' performance of the quadcopter. To validate the major contribution of this paper corresponding to improving the system's autonomy, the trajectory has been chosen as a horizontal flight with different fly speeds in each flight test. Moreover, the system orientation was imposed in the direction of the flight. Under this scenario, it is possible to assume that the later velocity  $v_{y,b/i}^b$  is negligible. This holds as long as Assumption 1 holds. Therefore, this makes it true to assume that additional forces in the lateral axis are negligible. As a result, the estimation of  $c_{y,q}$  coefficient is not considered in this paper. After we estimate the additional forces acting on the system, we can derive the quadcopter's propeller performance and fuselage aerodynamic models as described in the following subsections.

### 1. Propellers' Drag Model Identification

To estimate the parameter  $\lambda_p$ , we consider the outdoor experimentation for the Magnus-free quadcopter system at the low flying speed of  $2m.s^{-1}$ . This makes it true to ignore the aerodynamic effects encountered by the quadcopter body  ${}^a\mathbf{F}_q^b$ . An estimate  $\hat{\lambda}_p$  can then be derived by reformulating (22) as a least-squares system identification problem.

$$\hat{F}_{x,q}^b = -\hat{\lambda}_p v_{x,b/i}^b \quad (23)$$

For our quadcopter, the optimal estimate for this parameter is found to be 0.159. This parameter estimation process is executed once, and the resulting value is applied to the subsequent estimation task.

### 2. Quadcopter's Propellers' Performance and Fuselage Aerodynamics Model Identification

Considering the estimated parameter  $\hat{\lambda}_p$ , the quadcopter's fuselage aerodynamics and propellers' performance model are estimated by formulating (22) as a least-squares problem over the data collected from the experiments.  $exp \in \{2m.s^{-1}, 6m.s^{-1}, 8m.s^{-1}, 10m.s^{-1}\}$ :

$$\begin{cases} \hat{c}_{x,q} = \arg \min_{c_{x,q}} \sum_{exp} \| {}^{exp}\hat{\mathbf{F}}_x + c_{x,q} {}^{exp}\mathbf{v}_x \cdot \hat{\lambda}_p {}^{exp}\mathbf{v}_x \|^2 \\ (\hat{\lambda}_{T_1}, \hat{\lambda}_{T_2}) = \arg \min_{\lambda_{T_1}, \lambda_{T_2}} \sum_{exp} \| {}^{exp}\hat{\mathbf{F}}_z + c_{z,q} {}^{exp}\mathbf{v}_z \cdot \hat{\lambda}_p {}^{exp}\mathbf{v}_z \|^2 \\ - \left( \hat{\lambda}_{T_1} {}^{exp}\mathbf{v}_z - \hat{\lambda}_{T_2} {}^{exp}\mathbf{v}_z \cdot \hat{\lambda}_p {}^{exp}\mathbf{v}_z \right) \sum_k {}^{exp}\mathbf{w}_k \cdot \hat{\lambda}_p {}^{exp}\mathbf{v}_z \|^2 \end{cases} \quad (24)$$

such that  ${}^{exp}\hat{\mathbf{F}}_x$ ,  ${}^{exp}\hat{\mathbf{F}}_z$ ,  ${}^{exp}\mathbf{v}_x$ , and  ${}^{exp}\mathbf{v}_z$  are respectively the vector collection of the values  $\hat{F}_{x,q}^b$ ,  $\hat{F}_{z,q}^b$ ,  $v_{x,b/i}^b$ , and  $v_{z,b/i}^b$  in the stable region for each experiment  $exp \in \{2m.s^{-1}, 6m.s^{-1}, 8m.s^{-1}, 10m.s^{-1}\}$ . Similarly  ${}^{exp}\mathbf{w}_k$  denotes the collection of the  $k$ th propeller speed  $w_k$  values during each experiment  $exp$ . This work does not estimate the aerodynamic drag coefficient in  $z_b$ . Instead, this coefficient is taken to be  $C_{D_{z,q}} = 1.05$ , which is the drag coefficient of the cube. The estimated values we got are:  $\hat{c}_{x,q} = 0.0226$ ,  $\hat{\lambda}_{T_1} = 0.2212e-6$ , and  $\hat{\lambda}_{T_2} = 0.0753e-6$ . These identification processes are validated in Fig. 5. Such that the curves of the overall additional disturbance forces estimated according to the KF used

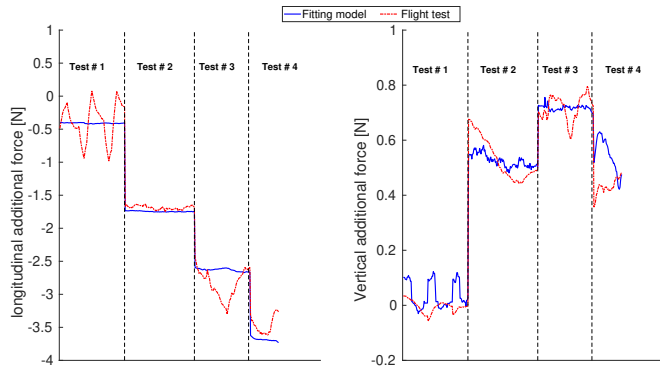


Fig. 5: Validation of the quadcopter propellers performance and aerodynamic models. From the figure, the red line corresponds to the additional forces estimated by implementing offline a KF on the system (20), and the blue line corresponds to the additional values predicted according to the derived model (22). The four separate flight tests are Test#1 (flight speed =  $2 \text{ m}\cdot\text{s}^{-1}$ ), Test#2 (flight speed =  $6 \text{ m}\cdot\text{s}^{-1}$ ), Test#3 (flight speed =  $8 \text{ m}\cdot\text{s}^{-1}$ ), and Test#4 (flight speed =  $10 \text{ m}\cdot\text{s}^{-1}$ ).

and described in this subsection (depicted in red) match that of the identified model (22)-(24) (depicted in blue).

## IV. Control Design

### A. Control Architecture

After presenting the system's dynamics, this section gives an overview of the control architecture. In this work, the overall control scheme is constructed as successive outer-inner closed loops: the position control loop, the optimization-based control allocation, and attitude control loops. The output of the innermost loop (low-level) is linked to the system's actuators. Fig. 6 summarizes the overall control architecture.

#### 1. Position Control Loop

Choosing the reference scenario for the outer position loop makes the approach general because any global path planner could supply the reference and extend the controller. Thus, the outer position loop controller is provided by the system's state, position  $\mathbf{p}_{r/i}^i$ , and velocity  $\mathbf{v}_{r/i}^i$  references. This loop computes the desired force vector  $\mathbf{F}_d$  necessary to stabilize and control the system. Different control strategies could be applied to this loop. In the present work, we design this position control loop as a proportional, integral, derivative (PID) controller. The integral action makes the system more robust to uncertainties and low-frequency changes in the experimental parameters.

#### 2. Optimization-Based Control Allocation

The design and implementation of this control loop will be described in detail in Section V. The control allocation receives the desired force vector  $\mathbf{F}_d$  from the position loop. The control allocation allocates this virtual

command between the Magnus's lift and the quadcopter's thrust. Thus, it outputs the desired Magnus spinning ratio  $X_d$ , the desired thrust  $T_d$ , and the desired attitude  $\Theta_d$ . A simplified aerodynamic model of the Magnus-effect based wing derived from the literature that captures the overall dynamics has been implemented. This makes it more suitable for the real-time controller application. Due to the computational demand of the numerical optimization involved in the control allocation strategy.

### 3. Attitude Controller

The control allocation loop supplies the desired attitude  $\Theta_d$  at a rate of 50Hz to the attitude loop. The attitude is controlled by the embedded attitude loop of the PX4 autopilot implemented onboard the quadcopter. This attitude control is implemented as a cascaded P/PID controller where the outer loop calculates the desired attitude rate  $\dot{\Theta}_d$ , which is used as an input to the inner attitude-rate control loop. This design allows a high update rate of 500 Hz and a high bandwidth in turn. Therefore, the bandwidth of the attitude control loop is significantly higher than the bandwidth of the outer position control loop. Then, the position controller, in this work, is designed to be largely independent of the dynamics of the attitude.

### B. Control Design Model

The translational dynamics involve four control variables: quadcopter thrust force  $T_c$ , two Euler angles (pitch  $\theta_c$  and roll  $\phi_c$  angles), and the spin ratio  $X_c$  of the Magnus-effect based wings. It might be premature to establish the values of the four variables based on the desired three-dimensional acceleration. This difficulty arises from the challenge of acquiring the constraint for these control variables. To this end, we must distinguish between two scenarios: the Magnus-free quadcopter described in Subsection C where we consider that the Magnus is disattached, and the quadcopter controls the system. The other scenario is the optimized spinning Magnus scenario, where the control contribution is allocated between the quadcopter and Magnus-effect based wings while considering the necessary constraints. This scenario will be discussed in detail in Section V. For the control design, we rely on the following assumptions,

ASSUMPTION 2. *The base vectors of  $\mathcal{M}_l$  and  $\mathcal{M}_r$  are parallel, and the two origins  $M_l$  and  $M_r$  in conjunction with the center of mass of MWQ system, share a common alignment,*

ASSUMPTION 3. *The aerodynamic forces produced by the left and right Magnus-effect based wings are equal and parallel in direction. And both are exposed with equal rotation velocity  $\omega_{m/b}$ .*

This enables us to simplify the problem into one Magnus cylinder  $\mathcal{M}(M_m, \mathbf{x}_m, \mathbf{y}_m, z_m)$  of a total surface area  $S_m = S_r + S_l$ , with its origin coincident with the center

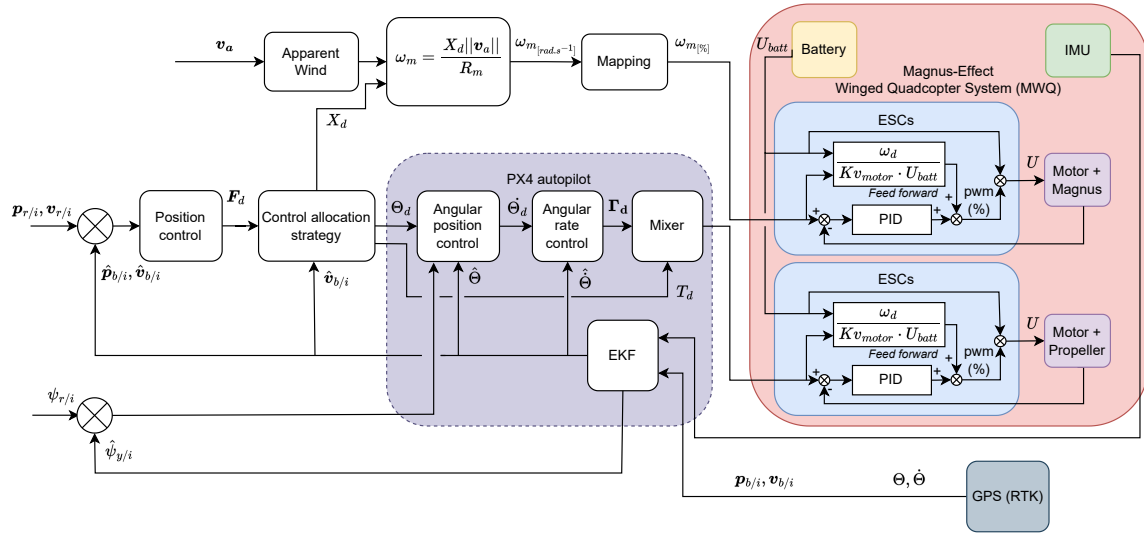


Fig. 6: An overview of the control scheme of the MWQ system. The outer position control loop computes the desired control contribution  $F_d$ . The control allocation strategy generates the commanded spin ratio of the Magnus and the commanded signals of the quadcopter. The inner loop of the PX4 autopilot controls the system's angular positions. All the rotational speeds of the motors are controlled through ESC.

of gravity of the MWQ system. The net aerodynamic moment of the Magnus-effect based wings is assumed to be negligible. Knowing that the centers of gravity  $M_r$  and  $M_l$  of the right and left Magnus-based wings, respectively, are symmetric with respect to the system's center of gravity, this assumption holds if Assumptions 2 and 3 hold.

This also lets us write the lift and drag forces produced by the Magnus-effect based wings in the longitudinal plane of the body frame  $\mathcal{B}$ ,

$${}^D \mathbf{F}_m^b = \frac{1}{2} \rho S_m c_{D_m} \|\mathbf{v}_{xz,b/i}\|^2 \mathbf{e}_D \quad (25a)$$

$${}^L \mathbf{F}_m^b = \frac{1}{2} \rho S_m c_{L_m} \|\mathbf{v}_{xz,b/i}\|^2 \mathbf{e}_L \quad (25b)$$

$${}^a \mathbf{F}_m^b := {}^a \mathbf{F}_m^b(X, \mathbf{v}_{b/i}^b) = {}^D \mathbf{F}_m^b + {}^L \mathbf{F}_m^b \quad (25c)$$

such that the drag  $\mathbf{e}_D$  and lift  $\mathbf{e}_L$  direction vectors are defined as,

$$\mathbf{e}_D = -\frac{\mathbf{v}_{xz,b/i}^b}{\|\mathbf{v}_{xz,b/i}^b\|}, \quad \mathbf{e}_L = \mathbf{y}_m \times \mathbf{e}_D \quad (26)$$

The lateral aerodynamic force produced by the Magnus-effect based wings is,

$${}^y \mathbf{F}_m^b = \frac{1}{2} \rho S_{m_y} c_{D_{m_y}} \|\mathbf{v}_{y,b/i}^b\|^2 \mathbf{y}_m \quad (27)$$

According to the above considerations and assuming that all additional forces acting on the system are regarded as disturbances, we can reformulate the lateral dynamics of the system (3) in the form:

$$\begin{aligned} \dot{\mathbf{p}}_{b/i}^i &= \mathbf{v}_{b/i}^i \\ \dot{\mathbf{v}}_{b/i}^i &= \mathbf{g}^i + \frac{1}{m} \mathbf{F}_c^i + \mathbf{d} \end{aligned} \quad (28)$$

The force vector  $\mathbf{F}_c$  is the vector of applied control forces and is considered as,

$$\mathbf{F}_c^i = R_c^i \left( \begin{bmatrix} 0 \\ 0 \\ T_c \end{bmatrix} + \begin{bmatrix} {}^a \mathbf{F}_{x,m}^b(X_c, \mathbf{v}_{b/i}^b) \\ 0 \\ {}^a \mathbf{F}_{z,m}^b(X_c, \mathbf{v}_{b/i}^b) \end{bmatrix} \right) \quad (29)$$

$$\text{with } R_c^i := R_c^i(\phi_c, \theta_c, \psi_c)$$

and  $\mathbf{d}$  is the disturbance vector that consists of the lateral aerodynamic force of the Magnus-effect based wings  ${}^y \mathbf{F}_m^b$ , and the additional forces acting on the quadcopter system  $\mathbf{F}_q$ .

$$\mathbf{d}^i = R_b^i ({}^y \mathbf{F}_m^b + \mathbf{F}_q^b) \quad (30)$$

### C. Outer Position Control Loop

In addressing the trajectory tracking problem, our initial emphasis will be on finding the desired attitude  $R_d^i := R_d^i(\phi_d, \theta_d, \psi_d)$  that will orient the desired force  $\mathbf{F}_d^i$  to guide the system toward a specified position reference trajectory  $\mathbf{p}_{r/i}^i$  under a reference velocity  $\mathbf{v}_{r/i}^i$  and a yaw reference trajectory  $\psi_{r/i}$ . We begin by ignoring thrust angle constraints, so  $\mathbf{F}_d^i$  can be any vector in the inertial frame; thrust angle constraints are handled by the introduced optimization in Section V. The tracking error model is given by the position, velocity, and acceleration errors as follows,

$$\begin{aligned} \mathbf{e}_p^i &= \mathbf{p}_{b/i}^i - \mathbf{p}_{r/i}^i \\ \dot{\mathbf{e}}_p^i &= \mathbf{v}_{b/i}^i - \mathbf{v}_{r/i}^i \end{aligned} \quad (31)$$

In order to satisfy convergence of the tracking error to zero, i.e.,  $\lim_{t \rightarrow +\infty} \|\mathbf{e}_p^i\| = 0$ , the desired force  $\mathbf{F}_d^i$  for (28)

can be provided by a PID controller in the form

$$\mathbf{F}_d^i = m(-\mathbf{g} - K_d \dot{\mathbf{e}}_p^i - K_p \mathbf{e}_p^i - K_i \int \mathbf{e}_p^i d\tau) \quad (32)$$

where  $K_d, K_p, K_i \in \mathbb{R}^{3 \times 3}$  are diagonal matrices acting respectively as the derivative, proportional, and integral control gains. Integral action improves the trajectory tracking performance in the presence of the neglected disturbance forces  $\mathbf{d}$  acting on the system.

The system's nose is chosen to be consistent with the direction of the system velocity, that is

$$\psi_{r/i} = \tan^{-1} \left( \frac{\dot{p}_{y,r/i}^i}{\dot{p}_{x,r/i}^i} \right) \quad (33)$$

We impose the desired yaw angle as  $\psi_d = \psi_{r/i}$ . After computing the desired force vector  $\mathbf{F}_d^i$ , we compute the desired thrust  $T_d$ , the desired pitch  $\theta_d$ , and roll  $\phi_d$  angles that enable the system to compensate for  $\mathbf{F}_d^i$ .

### 1. Magnus-free Quadcopter Configuration

For the scenario of disattached Magnus-effect based wings, the control force  $\mathbf{F}_c$  in (29) is reduced to  $\mathbf{F}_c = T_c R_c^i \mathbf{e}_3$ . Thus, the desired values  $T_d$  and  $R_d^i$  should satisfy the relationship:

$$\mathbf{F}_d^i = T_d \mathbf{z}_d^i \quad (34)$$

where  $\mathbf{z}_d = R_d^i \mathbf{e}_3$  and  $\mathbf{F}_d^i$  is the desired force as (32). Since  $\mathbf{z}_d^i$  is a column of an orthogonal matrix, it satisfies  $\bar{\mathbf{z}}_d^i \mathbf{z}_d^i = 1$ . Thus, it is further presented as

$$\mathbf{z}_d^i = \frac{\mathbf{F}_d^i}{\|\mathbf{F}_d^i\|} \quad (35)$$

Referring to equation (2), the vector  $\mathbf{z}_d^i$  can be expressed as:

$$\mathbf{z}_d^i = \begin{bmatrix} \cos \psi_d \sin \theta_d \cos \phi_d + \sin \psi_d \sin \phi_d \\ \sin \psi_d \sin \theta_d \cos \phi_d - \cos \psi_d \sin \phi_d \\ \cos \theta_d \cos \phi_d \end{bmatrix} = \frac{1}{\|\mathbf{F}_d^i\|} \begin{bmatrix} F_{x,d}^i \\ F_{y,d}^i \\ F_{z,d}^i \end{bmatrix} \quad (36)$$

Given that the vector  $\mathbf{z}_d^i$  has been determined through the earlier controller design, we can derive from (36) the following,

$$\begin{aligned} \theta_d &= \arctan 2 (F_{x,d}^i \cos \psi_d + F_{y,d}^i \sin \psi_d, F_{z,d}^i) \\ \phi_d &= \arcsin \left( \frac{F_{x,d}^i \sin \psi_d - F_{y,d}^i \cos \psi_d}{\|\mathbf{F}_d^i\|} \right) \end{aligned} \quad (37)$$

Considering  $T_d$  and  $\mathbf{z}_d^i$ , based on equation (34), we arrive at:

$$T_d = \bar{\mathbf{z}}_d^i \mathbf{F}_d^i \quad (38)$$

## V. Control Allocation Strategy For Energy Saving Performance

Energy saving is feasible for the Magnus-effect winged quadrotor system in transition flight mode. The underlying concept here involves maximizing the utilization of aerodynamical forces generated by two Magnus-effect based wings to take on the majority of the control duties. This approach is favored due to the energy-efficient

nature of controlling the Magnus rotation speed compared to the quadcopter's rotors control. Consequently, a cooperative control strategy is implemented to achieve energy-saving goals. To this end, the control strategy is based on a nonlinear optimization problem to allocate the desired control force  $\mathbf{F}_d^i$ , computed within the outer position control loop in Section C, into the Magnus-effect based wings and quadcopter rotors. In the design of the optimization problem, we assume the system to be stable in terms of yaw, which is attributed to the inner attitude control loop. This, in turn, enables the definition of the desired force  $\mathbf{F}_d^y$  in the desired yaw frame as follows:

$$\mathbf{F}_d^y = R_i^y(\psi_{y/i}) \mathbf{F}_d^i \quad (39)$$

The decision variables of the considered optimization problem are the desired Magnus spin ratio  $X_d$  and the desired pitch angle  $\theta_{p/y}$  with respect to the desired yaw frame. Constraints ensure that  $\mathbf{F}_d^y$  can be achieved within the limits of the pitch angle, the Magnus rotation speed, the quadcopter thrust force, and on the rate of change of the rotational speed of the Magnus-effect based wings.

The cost function of the optimization problem is designed to minimize the total thrust required at a specific Magnus spinning  $X$  and flying speed  $\mathbf{v}_{b/i}$  combination. This thrust is approximated to be the force needed on the top of Magnus aerodynamic forces  ${}^a \mathbf{F}_m$  to match the desired force  $\mathbf{F}_d$ . Therefore, the desired thrust in the desired pitch frame is defined as,

$$\begin{aligned} {}^t \mathbf{F}_d^p &= R_y^p(\theta) \mathbf{F}_d^y - {}^a \mathbf{F}_m^p(X, \mathbf{v}_{b/i}^p) \\ \mathbf{v}_{b/i}^p &= R_y^p(\theta) \mathbf{v}_{b/i}^y \end{aligned} \quad (40)$$

such that the desired thrust Magnitude  $T_d = \|\mathbf{F}_d^p\|$ .

Hence, the corresponding thrust cost function is defined as follows,

$$J_T := J_T(X, \mathbf{v}_{b/i}, \theta) = \|\mathbf{F}_d^p\|^2 \quad (41)$$

To ensure that the pitch angle  $\theta$  satisfies the desired thrust direction, the corresponding theta cost function can be chosen to be as,

$$J_\theta := J_\theta(X, \mathbf{v}_{b/i}, \theta) = \left( \theta - \arctan 2({}^t F_{x,d}^p, {}^t F_{z,d}^p) \right)^2 \quad (42)$$

Finally, to ensure that the spin ratio of the Magnus-effect based wings is minimal when flying at low speed, a penalty term  $J_X$  is added to the cost function. A possible formulation of  $J_X$  is expressed in (43). In this formulation, the penalty term becomes significant when the speed is low, and  $X$  is not near zero.

$$J_X := J_X(X, \mathbf{v}_{b/i}) = \frac{1}{\max(\epsilon, \|\mathbf{v}_{b/i}\|)} X \quad (43)$$

where  $\epsilon$  is a small enough parameter that is considered to avoid singularity. Finally, the cost functions represented in (40)-(43) are combined into a general cost function  $J_{tot}$  through the use of a vector  $\gamma$  of the weight coefficients

$$J_{tot} := J_{tot}(X, \mathbf{v}_{b/i}, \theta) = \gamma * [J_T \quad J_\theta \quad J_X]^T \quad (44)$$

The primary goal of the optimization problem is to allocate the control contribution between quadcopter and

Magnus-effect based wings to maximize energy efficiency. Therefore, the biggest weight is assigned to  $J_T$ . The pitch angle  $\theta_{p/y}$  determines the direction of the quadcopter's thrust. Therefore, failing to specify desired signals of  $\theta$  will lead to loss of altitude. It follows that  $J_\theta$  is assigned with important weight. Lastly, the lowest weight is assigned to  $J_X$ .

The optimization problem is then formulated as follows,

$$\begin{aligned}
&\text{given} && \mathbf{v}_{b/i}^y, \mathbf{F}_d^y \\
&\text{minimize}_{X_d, \theta_{p/y}} && J_{tot}(X_d, \mathbf{v}_{b/i}, \theta_{p/y}) \\
&\text{subject to} && \theta_{min} \leq \theta_{p/y} \leq \theta_{max} \\
& && w_{min} \leq w_{m/p} \leq w_{max} \\
& && T_{min} \leq T_d \leq T_{max} \\
& && |w_m - w_{m_{prev}}| \leq \delta w_{max}
\end{aligned} \tag{45}$$

The optimization problem (45) is solved using the interior-point optimization algorithm. As the position control loop runs in real-time, the solver must converge within the position loop's update period. If it is slow to converge to the optimal solution, we guarantee it is computing non-optimal but at least a solution that can achieve good performance.

The optimization will fail if the desired force  $\mathbf{F}_d$  vector falls beyond the attainable range while satisfying the constraints. To respect the constraints, we avoided dynamically infeasible scenarios when we planned the trajectory. As a result, rapid acceleration and deceleration are avoided.

Once the optimal pitch  $\theta_{p/y}$  and thrust  $T_d = \|\mathbf{F}_d^p\|$  have been obtained, it is necessary to augment the desired system attitude to include desired roll  $\phi_{d/p}$ . To achieve stability or control in the presence of lateral forces potentially caused by factors like wind or other disturbances, back to (37), the desired roll angle is computed as follows,

$$\phi_{d/p} = \arcsin\left(-\frac{{}^t F_{y,d}^p}{T_d}\right) \tag{46}$$

An important control step is compensating for the desired thrust force before feeding it to the quadcopter's inner loops. The relation between the desired thrust force magnitude  $T_d$  and the normalized compensated desired thrust force magnitude  ${}^c T_d[\%]$  is chosen to be,

$${}^c T_{d[\%]} = \frac{\sqrt{\frac{T_d}{4c_T}} - w_{min}}{w_{max} - w_{min}} \tag{47}$$

To validate our choice, we can compare, back to Fig. 4, the curve corresponding to (47) (depicted in green) to that corresponding to the thrust model (depicted in blue). These curves are shown to fit, which implies that the model we choose can serve for thrust calibration.

## A. Magnus-Effect Based Wing's Aerodynamic Model

As the optimization-based control allocation strategy is designed depending on the aerodynamic force  ${}^a \mathbf{F}_m$

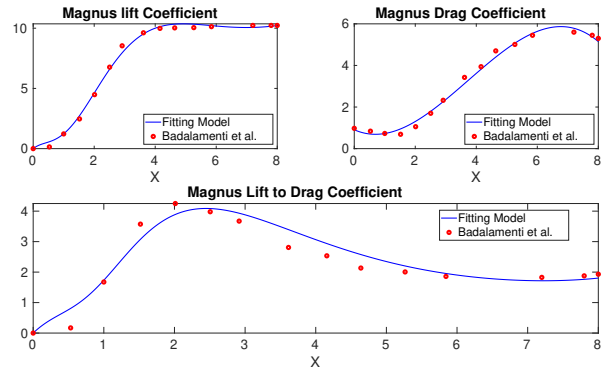


Fig. 7: Lift, Drag, and Lift-to-Drag coefficients of the Magnus-effect based wing as a function of spin ratio  $X$ . From the figure, the red dots correspond to the data taken from Badalamenti [17], and the blue line corresponds to the model fitted by (48)

generated by the Magnus-effect based wings, it is important to understand the behavior of wings' aerodynamics. In this present study, the aerodynamic model of the Magnus-effect based wings is derived from the data provided in [17]. This is applicable because we design the wings to have an Aspect ratio  $\Lambda = \frac{L_m}{2R_m} = 5.1$  equal to that in [17]. We have incorporated endplates into both wings. This addition significantly enhances lift and improves the lift-to-drag ratio while maintaining a small Aspect ratio. The diameter of the endplates is chosen to be twice that of the Magnus cylinder. To capture the general trend for lift and drag coefficients of the Magnus cylinder  $c_{L_m}$  and  $c_{D_m}$  respectively, the following prediction model is considered:

$$\begin{aligned}
c_{L_m} &= \left(1 - \frac{1}{1 + \exp(-0.904X)}\right) (0.0276X^4 + 4.6595X^3 \\
&\quad - 6.0369X^2 + 2.9557X) + \frac{1.0849X}{1 + \exp(-0.904X)}, \\
c_{D_m} &= -0.0461X^3 + 0.5167X^2 - 0.6511X + 0.9081
\end{aligned} \tag{48}$$

Fig. 7 presents the selection of aerodynamic coefficients that are available in the literature [17] and those predicted for the same range of spin ratios according to (48).

To gain a deeper insight into the performance derived from the control allocation strategy, we present, in Fig. 8, a 3D contour plot of the values of the cost function  $J_{tot}$ . In this context, we make the assumption that the desired force  $\mathbf{F}_d^i = mg$ . Consequently, while we can project a similar trend in experimentation, it is important to note that the exact values may not precisely align with our predictions. The figure's initial observation is evident: as the linear flight speed increases, the cost function takes on lower values (appearing as a darker shade of blue). This phenomenon is attributed to the Magnus effect, enabling higher lift force generation. Consequently, less thrust is required by the quadcopter to lift the system,

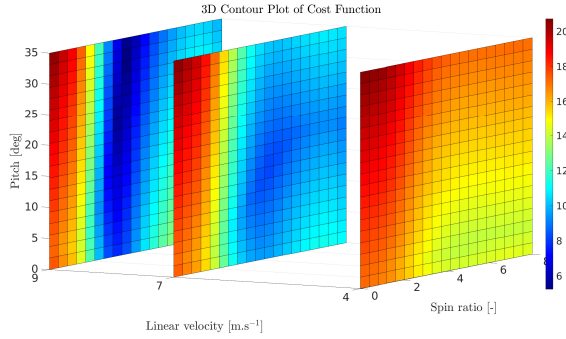


Fig. 8: Contour plot of the cost function of the control allocation strategy. Each color block represents a different value of the cost function.

resulting in a reduced value for the cost function. Another notable observation is the computation of the required spin ratio for the Magnus-effect based wings. This is done to achieve increased lift at lower flight speeds. Conversely, as the speed increases, the required spin ratio decreases. This adjustment aims to attain a balance between lift and drag, involving the rotation of the Magnus with a spin ratio around the one that results in maximal efficiency ( $X$  between 2 and 3, as seen in the Magnus, lift-to-drag coefficient in Fig. 7). Finally, the pitch angle increases with flight speed to compensate for the increased drag force generated due to the Magnus rotation.

The validation of the control allocation strategy effectiveness in achieving the desired thrust force reduction is conducted in Section VI. The assessment involves comparing energy-based results, including thrust force and consumed power, between the MWQ system with the control allocation strategy and a Magnus-free quadcopter controlled by the linear position control method from Subsection 1.

## VI. Validation

The validation of the control allocation strategy detailed in the previous section is undertaken through a two-phase process. First, we validate the controller through the realistic simulator described and validated in our previous work [23]. To enhance the realism of this simulation, critical factors such as the performance characteristics of the quadcopter propellers and the aerodynamic model of the quadcopter fuselage, as described in Subsection B, are considered in the simulation. Following the simulation phase, the strategy's validation extends to outdoor flight tests.

### A. Experimental Setup

Table I represents the involved parameters of the system. Our custom-built quadcopter is controlled by a Holybro Pixhawk 4 flight controller running PX4 Autopilot. Offboard position control is performed on a ground station through the Simulink Desktop Real-

Time toolbox. Communication between the MWQ system and the ground station is established using the Mavlink protocol over WiFi. A GPS receiver provides position measurements to conduct outdoor flights. We used the satellite navigation technique RTK GPS, which stands for Real-Time Kinematic Global Positioning System, to enhance the precision of position data obtained from standard GPS systems. A 4S LiPo battery supplies the quadcopter. Refer to Table II for a comprehensive list of all materials used, and see Fig. 9 for a representation of the experimental setup.

Parameter	Description	Value
$\rho$	Air density	$1.2930 \text{ kg.m}^{-3}$
$g$	Gravitational constant	$9.8100 \text{ m.s}^{-2}$
$m$	Total mass	$1.7660 \text{ kg}$
$m_q$	Quadcopter mass	$1.4450 \text{ kg}$
$L_m$	Magnus cylinder length	$0.5600 \text{ m}$
$R_m$	Magnus cylinder radius	$0.0275 \text{ m}$
$D_e$	Endplate diameter	$0.1100 \text{ m}$
$S_m$	Magnus cylinder surface area	$0.0308 \text{ m}^2$
$S_{m_y}$	Magnus cylinder lateral surface area	$0.0095 \text{ m}^2$
$[\theta_{min}, \theta_{max}]$	Bounds on pitch angle	$[-35^\circ, 35^\circ]$
$[w_{min}, w_{max}]$	Bounds on motors' rotational speed	$[0, 24000] \text{ rpm}$
$[T_{min}, T_{max}]$	Bounds on quadcopter's thrust	$[0.5, 34] \text{ N}$

TABLE I: Model Parameters

An ESC (Electronic Speed Controller) performs power driving of the brushless motor. The ESC is meant to apply a fraction of the battery voltage to the motor. This fraction is given by a standard digital input (most generally PWM or Dshot signal). Thus, the desired rotation speed of the motor is controlled via voltage regulation. In practice, there is a tendency for motors to run slower than expected as a result of air, dry friction, and battery voltage fluctuation. To ensure accurate speed control and precise force control for each motor, we have integrated custom firmware into conventional AM32 processor-based Electronic Speed Controllers (ESCs), enabling accurate closed-loop speed control. In our experimental configuration, the ESC input corresponds to a desired speed rather than a percentage of battery voltage. Speed control is executed within the ESC through a standard Proportional-Integral-Derivative (PID) regulator. Speed measurement involves monitoring the inversion of phase current in-

Item	Description
Flight controller	Holybro Pixhawk 4 with PX4 v1.14 firmware
Battery	Bashing 4S 5000mAh
Radiocontroller	FrSky Taranis X9D
RC receiver	FrSky XM+
Motor	T-Motor F60proV 1750 Kv
Propeller	AZURE POWER 6145 BPS
Propeller ESC	HGLRC 4in1 Zeus 45A (custom firmware)
Magnus cylinders	Chronics Technologies LWPLA cylinders
Magnus ESC	HGLRC T-Rex 35A (custom firmware)
Wifi Communication	ESP32 dev kit with serial/wifi bridge firmware
GPS	Drotek Sirius F9P Rover

TABLE II: Hardware setup

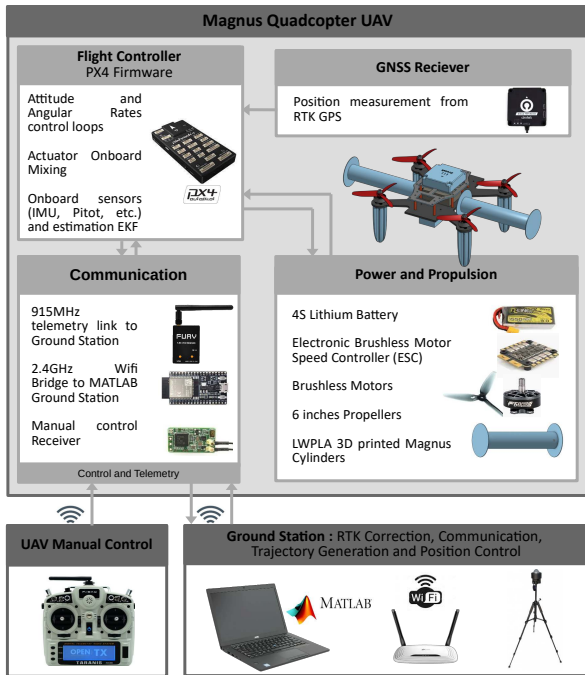


Fig. 9: The outdoor experimentation setup. From the figure, the main parts are the Quadcopter system, the Ground station, and the RTK GPS.

duced by the motion of rotor magnets. The ESC firmware that has been used is available at the website <sup>1</sup>.

## B. Results and Discussions

In this present paper, each flight experiment has been performed outdoor in an environment where wind speed is negligible, thus substantiating Assumption 1. The system precedes flight according to the following predefined flight plan, which is also described in Fig. 10

- **Step AB- Hovering:** The system performs autonomous hovering on site for a few seconds,
- **Step BC- From hovering to cruising flight:** after stationary hovering, the system starts accelerating in speed along the forward reference trajectory,
- **Step CD- Horizontal Flight:** After the flight speed reaches a different reference flight velocities at each test, the system cruises at the same speed to reach an absolute distance of 100m,
- **Step DE- From cruising to hovering:** Finally, the trajectory is followed by a decelerating horizontal flight.

In our investigation of a Magnus-effect winged quadcopter system MWQ controlled by a dynamic control allocation strategy, we systematically compared the performance at different flight speeds, specifically at  $4m.s^{-1}$ ,  $7m.s^{-1}$  and  $9m.s^{-1}$ . In the following discussions, in the presented figures red colored region corresponds to

accelerating phase, blue colored region corresponds to decelerating phase, and the region in between corresponds to the horizontal flight phase. In our discussions we focus only on these regions. Figs. 11 and 12 show the linear position and velocity profiles at these reference speeds. The position and velocity on every axis were successfully controlled, and they did not have large errors except during the deceleration phase. Larger tracking errors in the decelerating phase can be related to communication delays that we face during this phase at far distance. It may be also related to decelerating from high flight speed to the hovering phase being done very fast. This performance can be improved by extending the deceleration period. However, this requires wider land to achieve the same experiments presented in this paper, which was not available. Moreover, at  $9m.s^{-1}$ , we can observe a steady-state error in linear velocity attributed to the outer position control loop.

One important aspects to be analyzed for the MWQ system are the gyroscopic effect and the inertia counter-torque generated due the spinning of Magnus-effect based wings. As we mentioned earlier, these torques have been addressed and analyzed experimentally in our previous work [23]. To address these aspects through the experimental tests we presented in this paper, we plot Fig. 13 that highlights the gyroscopic effect and Fig. 14 which highlights the effect of inertia torque. Firstly, in Fig. 13, the low yaw rate during the flight tests at different flying speeds, talking about the acceleration, horizontal flight and deceleration phases, can be a key reason that the gyroscopic effect on the roll axis can be negligible. The variations shown for the desired roll angle can return to step movement along the sideways direction in order to start flying at a specific predefined starting point. This can be avoided by a better trajectory planning. But fortunately, this can be used in studying the gyroscopic effect on the yaw performance. The big variation on roll angle leads to higher roll rates that leads to gyroscopic effect on yaw axis. This is shown through the slightly imperfect tracking of the yaw angle. It is also important to mention that, by comparing the desired (depicted in red) and the measured (depicted in blue) roll and yaw angles, we can justify that the PID control of the attitude inner loops of the PX4 are well tuned and they are able to absorb the gyroscopic effect generated due to the rotation of the Magnus-effect based wings. Secondly, the variation of the rotational speed of the Magnus-effect based wings leads to inertial-counter torque on the lateral axis of the MWQ body, which is the axis of rotation of the Magnus cylinders. In order to analyse the effect of this torque, we plot in Fig. 14 the rate of change of the rotational speed of the Magnus-effect based wings as well as the pitch angle. Although the rotational speed of the Magnus-effect based wings show some high rates of change, no big effect is observed on the pitch angle. This justify that the inner attitude loops are able to absorb the inertia torque. These inner loops show good performance on pitch, which can be justified by the good fitting of the measured angle

<sup>1</sup><https://github.com/gipsa-lab-uav/AM32-MultiRotor-ESC-firmware>

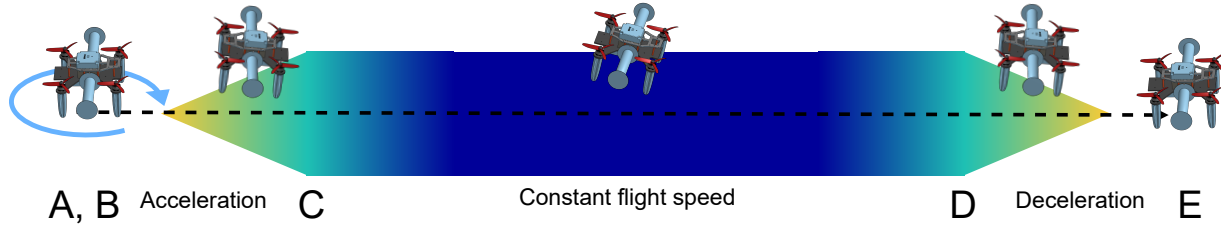


Fig. 10: The predefined flight plan for outdoor experimentation tests. From the figure, step AB is the hovering phase, step BC is the speed acceleration phase, step CD is the constant flight speed phase, and step DE is the speed deceleration phase

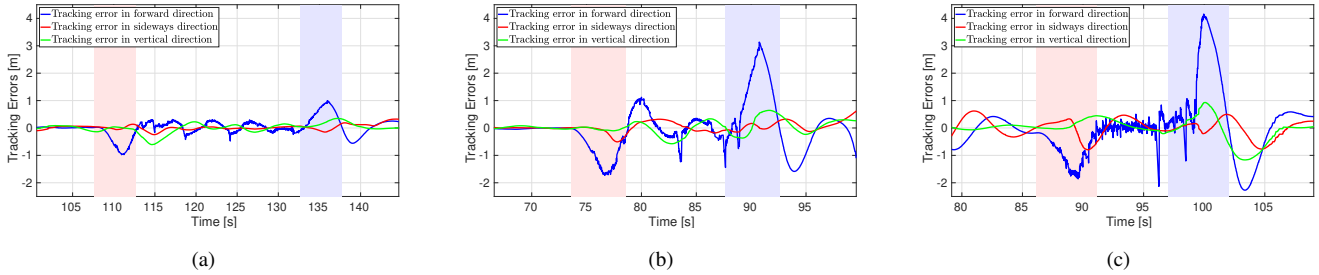


Fig. 11: Position tracking errors along the axes of the inertial frame. (a) corresponds to the flying speed of  $4m.s^{-1}$ , (b) corresponds to the flying speed of  $7m.s^{-1}$ , and (c) corresponds to the flying speed of  $9m.s^{-1}$ . From the figure, the blue line corresponds to the tracking error in  $x_i$ -direction, the red line corresponds to that in  $y_i$ -direction, and the green line corresponds to that in  $z_i$ -direction.

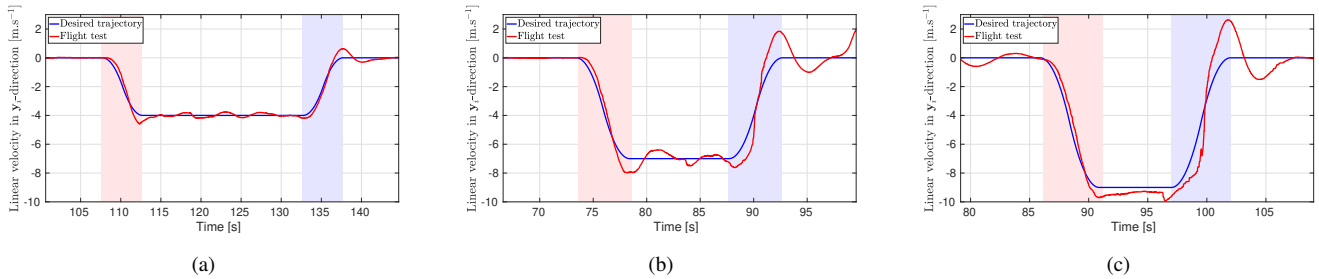


Fig. 12: Forward Linear velocity with respect to the inertial frame. (a) corresponds to the flying speed of  $4m.s^{-1}$ , (b) corresponds to the flying speed of  $7m.s^{-1}$ , and (c) corresponds to the flying speed of  $9m.s^{-1}$ . From the figure, the blue line corresponds to the reference linear speed, and the red line corresponds to the measured linear speed.

(depicted in blue) to that of the desired angle (depicted in red).

Building upon the insights gained from the 3D contour plot presented in Fig. 8, the command signals in Fig. 15 offer a more detailed view of the system's behavior under the online control allocation strategy in real flight test. Illustrated in the figure, the Magnus spin ratio exhibits dynamic behavior, initially rising from zero during hovering to prevent unnecessary power consumption when the Magnus contributes insignificantly to lifting the system. Subsequently, it adjusts to varying desired values at different flight speeds, decreasing as the flight speed

increases to find a balance between lift generation and drag forces.

Analyzing the Magnus spin ratio curves reveals essential patterns. During the deceleration phase, the spin ratio increases, indicating the control allocation strategy's intentional use of Magnus to enhance drag and aid in deceleration. Interestingly, the performance of the spin ratio contrasts with that of the pitch angle. At lower flight speeds, the Magnus spin ratio outperforms the pitch angle, reflecting the quadcopter's dominant role in system control. Conversely, the Magnus spin ratio becomes more influential at higher speeds.

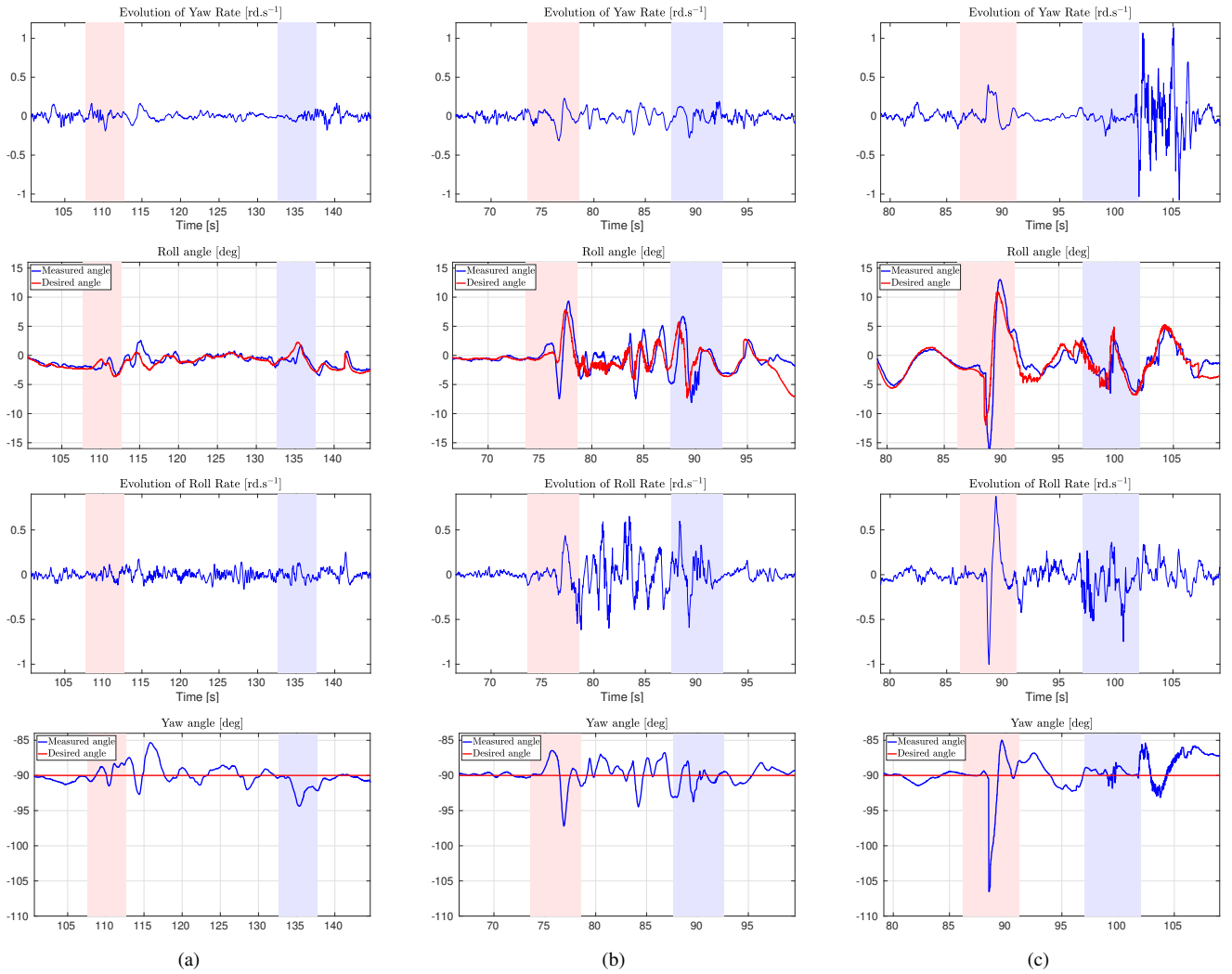


Fig. 13: Analysis of Magnus Gyroscopic Effect. From the figure, (a) corresponds to the flying speed of  $4m.s^{-1}$ , (b) corresponds to the flying speed of  $7m.s^{-1}$ , and (c) corresponds to the flying speed of  $9m.s^{-1}$ .

For broader flight speed range analysis, we gathered the stable performance regions for each flight speed, plotted in Fig. 16, which clearly shows the trend. In analyzing this figure, several key observations can be made. First, the behavior of the commanded Magnus spin ratio with respect to flight speed. At lower flight speeds, the commanded Magnus spin ratio aligns closely with values that result in maximal lift force (as seen in Fig. 7). However, as the flight speed increases, the commanded spin ratio decreases concurrently with an elevation in the commanded pitch angles. This adjustment in pitch angles is a strategic response to counteract the increased drag generated by the Magnus rotation and acting on the quadcopter fuselage, reaching saturation such that  $\theta = \theta_{max}$ , after a certain flight speed. Remarkably, the required quadcopter's thrust is minimal when the pitch angle is firstly saturated. Beyond the corresponding flight speed of this point, where the pitch has already saturated, a gradual rise in the commanded quadcopter's thrust can be noticed. The trend shown in Fig. 16, in other words the

minimal required thrust force and the corresponding flight speed, differs based on the saturation limit  $\theta_{max}$  of the pitch angle as well as the structural size of the system. In this study, the saturation limit  $\theta_{max}$  is imposed to  $35^\circ$  as identified in Table I, this is mainly because of two reasons. Firstly, to guarantee that the system is not approaching its physical limits for the seek of safety. The other reason is to be able to validate and present different performance scenarios, i.e., pitch is not saturated (flight speed lower than  $7m.s^{-1}$  in the current results) and pitch is saturated (flight speed equal or higher than  $7m.s^{-1}$  in the current results).

Fig. 16 demonstrates a strong matching between the simulation results (depicted in blue lines) and real outdoor flight tests (depicted in red dots). This holds despite knowing that the aerodynamic model of the Magnus-effect based wings utilized in the design of the control allocation strategy and the simulations may not precisely match their actual equivalents. This observation does not apply to thrust values, which is also demonstrated in Fig. 17

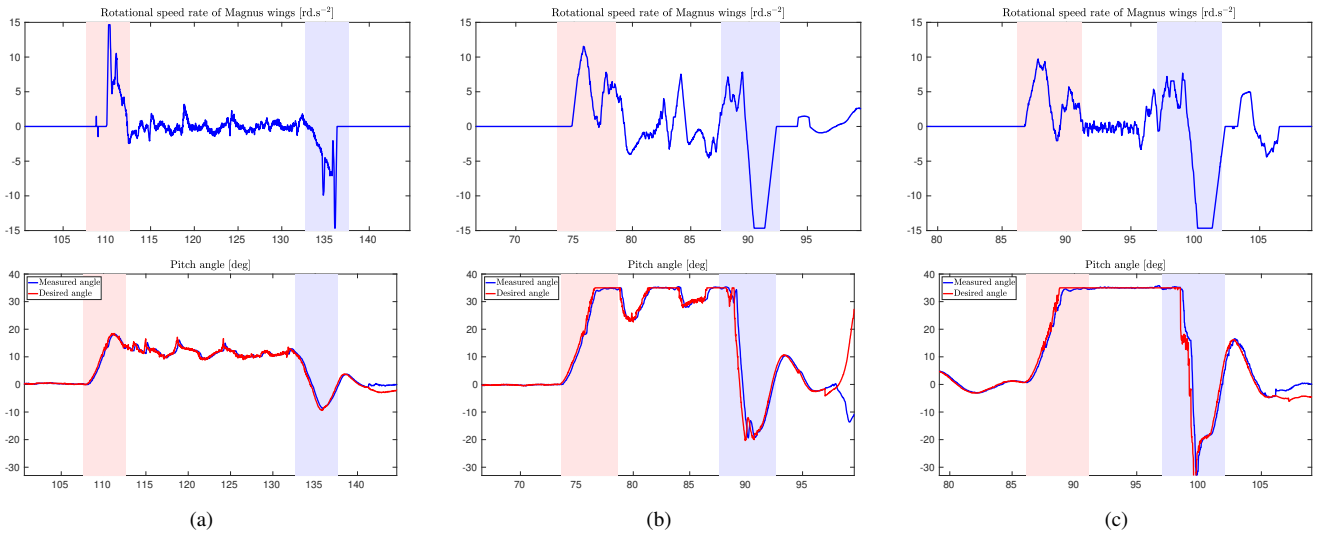


Fig. 14: Analysis of Inertial-Counter Torque. From the figure, (a) corresponds to the flying speed of  $4m.s^{-1}$ , (b) corresponds to the flying speed of  $7m.s^{-1}$ , and (c) corresponds to the flying speed of  $9m.s^{-1}$ .

(simulation thrust values depicted in dark blue dashed line and flight test values depicted in red dots). The mismatch of the simulated and real flight test thrust values is clearly shown at high flight speeds, for instance, at  $9.3m.s^{-1}$  we can record  $11.97N$  as the average thrust value of the flight test and  $14.46N$  as the thrust value of the simulation test. In addition to the possibility of aerodynamic modeling error of the wings, this thrust mismatch can also be highly related to the limitation of the identified quadcopter's propeller performance model (presented in Subsection B) at high local vertical speed  $v_{z,b/i}^b$ . This is because of the limited flight tests of the Magnus-free quadcopter. Fig. 17 also presents the thrust trend of the quadcopter through a flight test of the Magnus-free quadcopter system (depicted in orange dots). First, one can notice a good match between the flight test and simulation values (depicted in a light blue dashed line). This validates the quadcopter's drag and propeller performance model in the case of the Magnus-free quadcopter configuration described in Subsection B. Moreover, one interesting observation is the slight decrease and then increase of the thrust force. This brings us to the conclusion that the propulsion model used in simulations needs to take flight speed into account.

Figs. 17 and 18 offer valuable insights into the expected connection between power, quadcopter's thrust, and flight speed. Power and thrust exhibit a consistent trend as flight speed varies. Fig. 18 provides evidence of achieving our primary goal of enhancing system autonomy at higher flight speeds (achievable through reducing power consumption). The comparative analysis highlights the advantage of the control allocation strategy for the MWQ system, showcasing lower power consumption (depicted in blue) in contrast to the power required for conventional quadcopter flight without Magnus (depicted in red). From these figure, some main observations can be derived:

- Notably, during the hovering phase at  $0m.s^{-1}$ , the power demand for the MWQ system exceeds that of the quadcopter. This discrepancy is attributed to the Magnus effect not actively contributing during hovering, accompanied by the introduction of additional weight due to Magnus cylinders' motors.
- On the other hand, for a flight speed of  $4m.s^{-1}$ , although the commanded thrust is almost equal to that required for the quadcopter without the Magnus (as shown in Fig. 17), the system consumes higher power. The equal required quadcopter's thrust, at this flight speed, is analyzed such that the lift force generated by the rotating Magnus-effect based wings compensates for the additional weight. However, the higher power consumed by the MWQ is due to the additional energy required for rotating the Magnus cylinder at the commanded speed, underscoring the system's trend-offs.
- At flight speeds between  $0m.s^{-1}$  and  $7m.s^{-1}$ , there is a decrease in the required quadcopter's thrust and consumed power with the increase of flight speed, facilitated by the increased lift generated by Magnus rotation to compensate for the system's weight effectively. This dynamic reflects the efficacy of Magnus in altitude control at moderate flight speeds.
- However, the thrust and power consumption increase as the flight speed surpasses the optimal point (above  $7m.s^{-1}$  flight speed). This phenomenon is attributed to the increasing residual drag that, beyond the optimal speed, necessitates higher thrust for sustained flight.

The MWQ system, when controlled by the optimization-based control allocation, demonstrates more efficient power consumption and requires less thrust from the quadcopter for flight speeds between

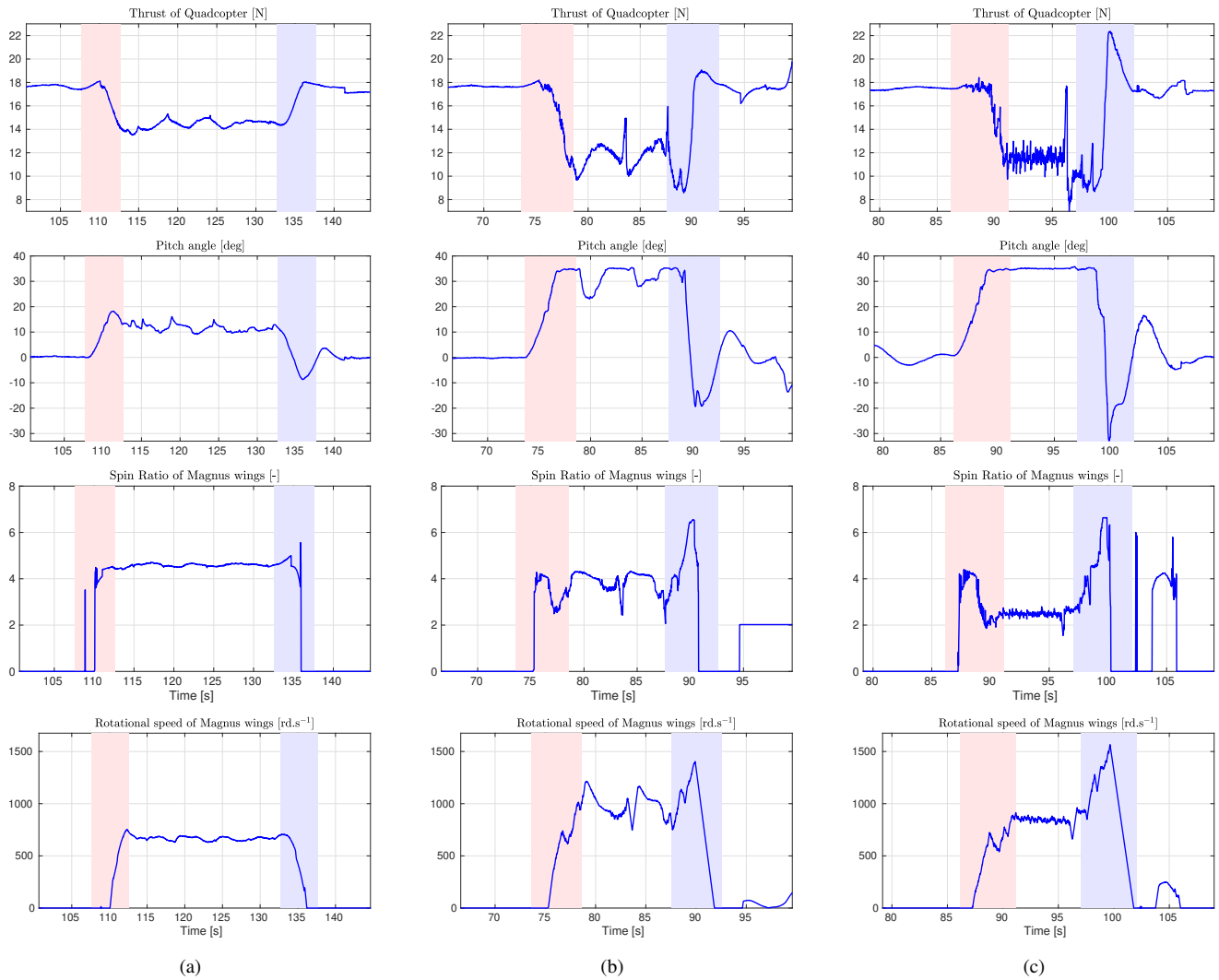


Fig. 15: The performance of the control variables. From the figure, (a) corresponds to the flying speed of  $4m.s^{-1}$ , (b) corresponds to the flying speed of  $7m.s^{-1}$ , and (c) corresponds to the flying speed of  $9m.s^{-1}$ .

$4m.s^{-1}$  and  $9.3m.s^{-1}$ . This efficiency is observed despite the higher aerodynamic disturbances experienced by the MWQ system compared to the Magnus-free quadcopter, which result from flying at higher pitch angles. However, it is predicted that at flight speeds above  $9.3m.s^{-1}$ , the thrust force required by the MWQ system would surpass that of the Magnus-free quadcopter after certain flight speed. This is due to increased aerodynamic disturbances at saturated pitch angles. Future work should integrate these aerodynamic disturbances into the optimization problem. Additionally, the effective flight range could vary based on several factors, such as the dimensions of the Magnus-effect-based wings, fuselage, and overall quadcopter design.

In the scope of this paper, it is important to note that structural analysis for optimizing the system's aerodynamics and, consequently, power consumption has not been addressed. Moreover, as mentioned before, the experimental tests presented and analyzed in this paper have

been performed under no wind and no wind gusts. To comment on this topic, in the case where Assumption 1 doesn't hold, the apparent speed  $v_a$  is considered as in (1), and the control strategy can be implemented with this formulation of the apparent speed. Thus, the additional aerodynamic forces generated due to the external wind speed  $v_w$  are not considered a part of the disturbances  $d$  but are considered in the control strategy. In the case when the system is subjected to wind gusts, we can predict that the MWQ system underperforms the Magnus-free quadcopter system, however it is more robust to wind gusts than the classical airfoil winged quadcopter system. This can be justified by the fact that the surface area subjected to relative wind is most compact in the Magnus-free quadcopter, followed by the MWQ system, and then the classical airfoil winged quadcopter system.

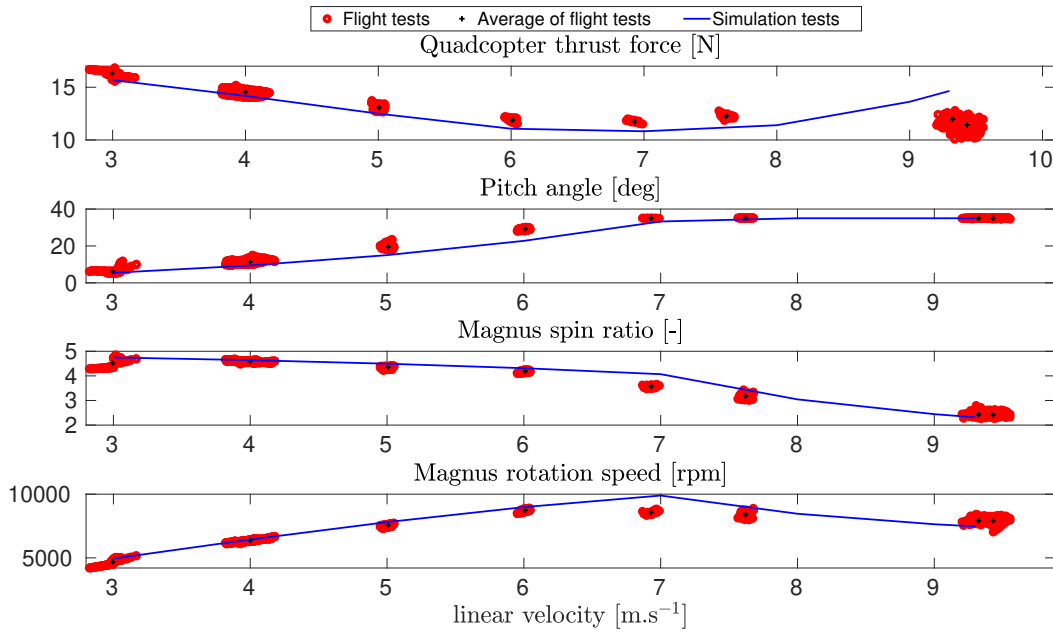


Fig. 16: The dynamical behavior of the control allocation strategy through outdoor flights and simulation tests at a wide range of flight speeds. From the figure, the red dots represent the data gathered at stable regions from the flight tests, and the blue line corresponds to the simulation data.

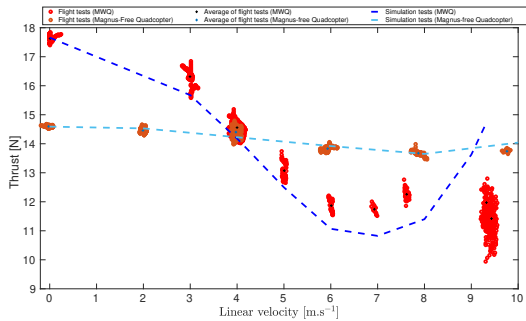


Fig. 17: Quadcopter thrust forces at different flight speeds validated in simulation and flight test. From the figure, the red dots and the dark blue dotted line correspond to the tests for the MWQ system controlled by the control allocation strategy, and the orange dots and light blue dotted line correspond to the tests for the Magnus-free quadcopter system

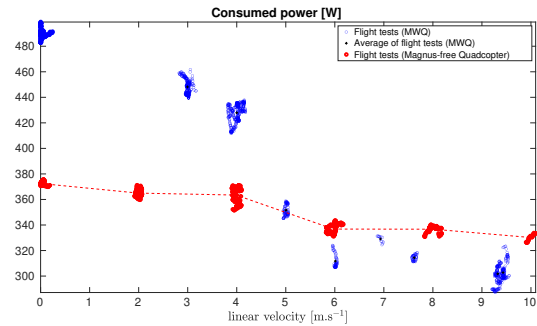


Fig. 18: Power consumed by the system during the outdoor flight tests. From the figure, the blue dots correspond to that consumed during the flight of the MWQ system controlled by the control allocation strategy, and the red dots correspond to the consumed power during the flight of the Magnus-free quadcopter system.

## VII. Conclusion and Future Work

This paper presents the modeling, controller design, and energy efficiency study of the Magnus-effect winged quadcopter system - a novel hybrid UAV system. Modeling is conducted by incorporating forces, including drag aerodynamics and propeller performance estimations based on prior outdoor experimental data for the quadcopter without Magnus-effect based wings. We design a hierarchical control strategy to control our system. The outer position control loop we adopt a model based feedback closed loop controller with integral action. This makes the controlled system more robust to uncertainties and low-frequency changes in the experimental param-

eters. The lower level control loop is designed as a nonlinear optimization-based control strategy to allocate thrust efficiently to maximize the Magnus-effect-based wings' lift contribution and minimize the quadcopter's thrust. This approach has been validated through several outdoor experimental tests. We believe this work will help in the design of future autopilots for different applications.

This study uses Magnus-effect based wings instead of a traditional airfoil. The decision was driven because of some qualitative aspects comparing the two wing configuration. Firstly, commenting on the control and robustness aspect, controlling lift generated by an airfoil often requires adjustments based on the angle of attack. In contrast, the Magnus effect provides a more robust

and straightforward control mechanism. Moreover, the aerodynamic characteristics of the Magnus-effect based wings make it more compact at relatively low flight speeds compared to classical airfoils. This can be justified knowing that the lift coefficient of the Magnus-effect based wing can reach a value about six times of that of the classical airfoil. Thus, the Magnus-effect based wings are more suitable for low flight speed application compared to classical airfoil configuration. We can also comment on the mechanical flexibility in attaching and disattaching the Magnus-effect based wings, thus making it more easy to repair them in case of crash.

To further generalize and enhance the performance of system, we still need to achieve different tasks and improvements in our future work. Firstly, to overcome the conservative assumption of zero wind, we will use a 3D pitot wind sensor. This will make us compute accurately the apparent speed which is fed to the optimization problem. We will also focus our future research on improving the control strategy's performance and robustness by integrating the proposed quadcopter's aerodynamic drag and propeller performance model as part of the position control loop. This necessitates the creation of a more accurate model of these disturbances. To this end, the whole disturbance could be estimated through an online disturbance observer. Moreover, since the proposed control strategy depends highly on the aerodynamic model, a more accurate model could enhance the controller's performance. We will conduct proper system identification and/or wind tunnel testing to obtain a proper aerodynamic model of the Magnus-effect based wings, which are, for now, based on a literature model. To consider different aspects affecting this model, we have to conduct tests under different wind speeds and different spin ratios of the Magnus cylinder.

One additional aspect that needs to be addressed in future experimental tests is improving the communication delay. In the experiments presented in this paper, we utilized the facilities available in our lab, and we acknowledge that these could be enhanced. Experimentally, we observed that significant communication delays can lead to degraded flight performance. Notably, higher communication delays were encountered at far distances during the decelerating phase, resulting in larger tracking errors. To enhance system performance, implementing an onboard embedded controller will be necessary.

## ACKNOWLEDGMENT

This work has been partially supported by ROBOTEX 2.0 (Grants ROBOTEX ANR-10-EQPX-44-01 and TIRREX ANR-21-ESRE-0015), funded by the French program Investissements d'avenir.

## REFERENCES

[1] X. Yang and X. Pei, "Hybrid system for powering unmanned aerial vehicles: Demonstration and study cases," *Hybrid Technologies for Power Generation*, pp. 439–473, 2022.

[2] A. S. Saeed, A. B. Younes, S. Islam, J. Dias, L. Seneviratne, and G. Cai, "A review on the platform design, dynamic modeling and control of hybrid uavs," *2015 International Conference on Unmanned Aircraft Systems (ICUAS)*, pp. 806–815, 2015.

[3] G. J. Ducard and M. Allenspach, "Review of designs and flight control techniques of hybrid and convertible vtol uavs," *Aerospace Science and Technology*, vol. 118, p. 107035, 2021.

[4] Q. Quan, *Introduction to multicopter design and control*. Springer, 2017.

[5] C. De Wagter and E. J. Smeur, "Control of a hybrid helicopter with wings," *International Journal of Micro Air Vehicles*, vol. 9, no. 3, pp. 209–217, 2017.

[6] C. Chen, J. Zhang, D. Zhang, and L. Shen, "Control and flight test of a tilt-rotor unmanned aerial vehicle," *International Journal of Advanced Robotic Systems*, vol. 14, no. 1, p. 1729881416678141, 2017.

[7] A. Misra, S. Jayachandran, S. Kenche, A. Katoch, A. Suresh, E. Gundabattini, S. K. Selvaraj, A. A. Legesse, *et al.*, "A review on vertical take-off and landing (vtol) tilt-rotor and tilt wing unmanned aerial vehicles (uavs)," *Journal of Engineering*, vol. 2022, 2022.

[8] J.-M. Kai, T. Hamel, and C. Samson, "A unified approach to fixed-wing aircraft path following guidance and control," *Automatica*, vol. 108, p. 108491, 2019.

[9] J. Zhou, X. Lyu, Z. Li, S. Shen, and F. Zhang, "A unified control method for quadrotor tail-sitter uavs in all flight modes: Hover, transition, and level flight," pp. 4835–4841, *IEEE*, 2017.

[10] Z. Li, W. Zhou, and H. Liu, "Robust controller design for a tail-sitter uav in flight mode transitions," in *2018 IEEE 14th International Conference on Control and Automation (ICCA)*, pp. 763–768, *IEEE*, 2018.

[11] L. Bauersfeld, L. Spannagl, G. J. Ducard, and C. H. Onder, "Mpc flight control for a tilt-rotor vtol aircraft," *IEEE Transactions on Aerospace and Electronic Systems*, vol. 57, no. 4, pp. 2395–2409, 2021.

[12] M. Allenspach and G. J. J. Ducard, "Nonlinear model predictive control and guidance for a propeller-tilting hybrid unmanned air vehicle," *Automatica*, vol. 132, p. 109790, 2021.

[13] D. Rohr, T. Stastny, S. Verling, and R. Siegwart, "Attitude and cruise control of a vtol tilting uav," *IEEE Robotics and Automation Letters*, vol. 4, no. 3, pp. 2683–2690, 2019.

[14] D. Rohr, M. Studiger, T. Stastny, N. R. Lawrance, and R. Siegwart, "Nonlinear model predictive velocity control of a vtol tilting uav," *IEEE Robotics and Automation Letters*, vol. 6, no. 3, pp. 5776–5783, 2021.

[15] J. B. Willis and R. W. Beard, "Nonlinear trajectory tracking control for winged evtol uavs," in *2021 American Control Conference (ACC)*, pp. 1687–1692, *IEEE*, 2021.

[16] K. Hansen, R. Kelso, and B. Dally, "The effect of leading edge tubercle geometry on the performance of different airfoils," *Proceedings of the 7th World Conference on Experimental Heat Transfer, Fluid Mechanics and Thermodynamics*, 2009.

[17] C. Badalamenti and S. Prince, "Effects of endplates on a rotating cylinder in crossflow," in *26th AIAA Applied Aerodynamics Conference*, p. 7063, 2008.

[18] J. Seifert, "A review of the magnus effect in aeronautics," *Progress in aerospace sciences*, vol. 55, pp. 17–45, 2012.

[19] A. Hably, J. Dumon, G. Smith, and P. Bellemain, "Control of a magnus effect-based airborne wind energy system," *Airborne Wind Energy: Advances in Technology Development and Research*, pp. 277–301, 2018.

[20] Z. Azaki, J. Dumon, N. Meslem, and A. Hably, "Sliding mode control of tethered drone: Take-off and landing under turbulent wind conditions," *2023 International Conference on Unmanned Aircraft Systems (ICUAS)*, pp. 769–774, 2023.

[21] W. Khan and M. Nahon, "Development and validation of a propeller slipstream model for unmanned aerial vehicles," *Journal of Aircraft*, vol. 52, no. 6, pp. 1985–1994, 2015.

- [22] H. Yeo and W. Johnson, "Performance and design investigation of heavy lift tilt-rotor with aerodynamic interference effects," *Journal of Aircraft*, vol. 46, no. 4, pp. 1231–1239, 2009.
- [23] Z. Azaki, P. Susbielle, A. Offermann, J. Dumon, N. Meslem, A. Hably, and A. Negre, "Experimentally validated simulator of flight dynamics: for a magnus effect-based quadcopter system," *International Micro Air Vehicles, Conferences and Competitions*, 2023.
- [24] J.-M. Kai, G. Allibert, M.-D. Hua, and T. Hamel, "Nonlinear feedback control of quadrotors exploiting first-order drag effects," *IFAC-PapersOnLine*, vol. 50, no. 1, pp. 8189–8195, 2017.
- [25] Y. Gupta, J. Dumon, and A. Hably, "Modeling and control of a magnus effect-based airborne wind energy system in crosswind maneuvers," *IFAC-PapersOnLine*, vol. 50, no. 1, pp. 13878–13885, 2017.
- [26] R. E. Kalman, "A new approach to linear filtering and prediction problems," *Transactions of the ASME—Journal of Basic Engineering*, vol. 82, no. Series D, pp. 35–45, 1960.



**Zakeye Azaki** received a M.S. degree in automatic, signal, and image processing from Paris-Saclay University and CentraleSupélec, Gif-sur-Yvette, France, in 2021. Currently, she is working toward the Ph.D. degree with the Grenoble Image Parole Signal Automatique Laboratory (GIPSA-Lab) and Grenoble Institute of technology of the Université Grenoble Alpes (UGA, Grenoble INP). Her research interests include robotics, nonlinear and predictive control, optimization, and airborne wind-energy systems.



**Jonathan Dumon** received a M.S. degree from Ecole Centrale de Nantes in system, image and signal processing specialization in 2002. After 4 years in the manufacture of special machines for industry, he joined CNRS in 2006 where he is now research engineer, in charge of aerial robotic platforms in the Grenoble Image Parole Signal Automatique Laboratory (GIPSA-Lab). His technical and research interests include mechatronics, robotics, wind turbines and airborne wind-energy systems.



**Alexis Offermann** received a M.S. degree in mechatronics from Université de Strasbourg in 2016 and then a Ph.D. degree from the University Technologique de Compiègne in 2021 in aerial robotics applied in the building inspection field. Since 2021, he has been a research engineer at the University of Compiègne and then at the University of Grenoble Alpes. He is a member of Gipsa-lab in the aerial robotic platform department. He conceived and manufactured a number of robots during his Ph.D. as well as during his activity as a research engineer.



**Nacim Meslem** received a M.S. degree from Ecole Centrale de Nantes in 2004 and then a Ph.D. degree in engineering sciences from the University of Paris Est Créteil in 2008 in the field of set theory applied to control system engineering. Since 2012, he has been an Associate Professor at the University of Grenoble Alpes, affiliated to ENSE3 (National School of Energy, Water and Environment) Grenoble, France. He is a member of automatic control department at Gipsa-lab. His research interests include set-valued estimation, event-based control and estimation, and airborne wind-energy systems.

control department at Gipsa-lab. His research interests include set-valued estimation, event-based control and estimation, and airborne wind-energy systems.



**Pierre Susbielle** received the B.E. degree in automation and mechatronics (specialized in serial robotics), from the Institute Polytechnique de Grenoble, Grenoble, France, in 2021. He joined the technical team of GIPSA-Lab (Grenoble Control Laboratory) as a research engineer. He contributes to the development of experimental platforms for aerial robotics, with research projects about artificial intelligence for the control, management and coordination of swarms of drones and complex aerial systems piloting.

coordination of swarms of drones and complex aerial systems piloting.



**Amaury Negre** graduated from the National Polytechnical Institute of Grenoble (INPG), France, in 2005, with a major in image processing. He received a PhD degree in vision and robotics from INPG, in 2009 for his work on vision based obstacle detection for mobile robots. He joined CNRS in 2008 where he is now a research engineer with the GIPSA-Lab and offers engineering and research support in aerial robotics.



**Ahmad Hably** received a M.S. degree and the Ph.D. degree in automatic control from the Grenoble Institute of Technology, Grenoble, France, in 2005 and 2007, respectively. Since 2008, he is an Associate Professor with the Grenoble Image Parole Signal Automatique Laboratory (GIPSA-Lab) and Grenoble Institute of technology of the Université Grenoble Alpes (UGA, Grenoble INP). His research interests include nonlinear control, optimization, renewable energy and airborne wind-energy systems.

renewable energy and airborne wind-energy systems.